THESIS

LARGE-SCALE REMOTE SENSING OF GEOMORPHIC CHANGE IN MULCHED AND UNMULCHED WATERSHEDS BURNED IN THE 2020 EAST TROUBLESOME FIRE, COLORADO

Submitted by

John Thomas Murray

Department of Civil and Environmental Engineering

In partial fulfillment of the requirements

For the Degree of Master of Science

Colorado State University

Fort Collins, Colorado

Summer 2023

Master's Committee:

Advisor: Peter Nelson

Stephanie Kampf
Ryan Morrison

ABSTRACT

LARGE-SCALE REMOTE SENSING OF GEOMORPHIC CHANGE IN MULCHED AND UNMULCHED WATERSHEDS BURNED IN THE 2020 EAST TROUBLESOME FIRE, COLORADO

Elevated levels of sediment transport in post-wildfire landscapes can degrade the hydrologic and geomorphic processes of a river system, damage aquatic habitat, and pose a threat to downstream infrastructure. Hillslope mulching applications have proven to be effective at mitigating runoff and erosion at plot and hillslope scales but the impacts of mulching at the watershed scale remain generally unknown. We conducted repeat aerial surveys of one unmulched and five partially mulched watershed outlets (0.61-1.44 km^2) to quantify erosion and deposition in the East Troublesome Fire burn scar. The objectives of the study were (1) to quantify volumes of erosion and deposition for hillslopes and channels for a variety of sites at a range of elevations (2) to identify and quantify the drivers of erosion and deposition and their relative contributions within and across watersheds (3) to determine the impact of slope, width, and vegetation cover on sediment storage and transport within watersheds; and (4) to assess the impacts of a large-scale aerial mulching operation at scales from hillslopes to watersheds. Multiple drone flights were conducted for each study site between July and October 2022. The earliest and latest surveys were differenced to produce DEM of Difference (DoD), with spatial resolutions ranging from 3.8 to 4.4 cm. Vertical uncertainties calculated from measurement uncertainty and Structure from Motion (SfM) errors were filtered out of the DoD at a 95% confidence interval (CI), resulting in maximum and mean detection thresholds of 11 and 4 cm, respectively. A supervised

classification algorithm was used to filter out changes due to vegetation growth and decay, which varied in effectiveness across the six study sites. Hillslope erosion and deposition volumes were at least three times higher than near-channel volumes, with most sites being an order of magnitude higher. However, near-channel erosion and deposition magnitudes normalized by area were higher than normalized hillslope magnitudes at all sites. A bootstrap forest regression model was used to determine relationships between various site-specific parameters and erosion and deposition for each watershed individually, and for all six sites combined. The model indicated mean slope, absence of vegetation, mean differenced normalized burn ration (dNBR), and hillslope length to be strong drivers of erosion and deposition for the individual models. Total precipitation accumulation and maximum 60-minute rainfall intensity were stronger contributors in the combined models. Near-channel storage and transport was influenced by local relationships between width, stream power, and absence of vegetation. Mulch coverage area was found to be weakly correlated with erosion and deposition at the watershed scale, with contributions possibly being dependent on coverage rate. These findings emphasize the importance of applying mulch in areas where it is both necessary and can have a measurable impact on reducing erosion rates.

ACKNOWLEDGEMENTS

I would first like to thank the Colorado Water Conservation Board and Northern Water for their support of this project, without whom projects aimed at protecting our valuable natural resources, such as this one, would not be possible. I would also like to acknowledge my committee members Stephanie Kampf and Ryan Morrison, who provided support and guidance that was crucial to the success of this study. Next, I must extend the utmost gratitude to my advisor, Peter Nelson. I could not have finished this project without his constant support, patience, and knowledge, for which I will always be grateful. I would like to thank Lindsey Hayter and Cameron Turnbow for helping in the collection and processing of data, and for participating in countless brainstorm sessions that I will look back on fondly for a long time. Lastly, I would be remiss if I did not thank my friends and family who supported me the entire way, and always made sure to remind me where I am from.

TABLE OF CONTENTS

(1) INTRODUCTION

Wildfire prone regions, including the Colorado Front Range, are experiencing accelerated rates of large-scale, high-burn-severity wildfires. This increase in scale and severity has been linked to historic fire suppression and droughts attributed to climate change (Westerling et al., 2006; Miller et al., 2009). Wildfires enhance surface runoff and transport of surface sediment and debris by decreasing surface roughness and soil permeability and increasing ground litter (Benavides-Solorio and Macdonald, 2001, 2005; Robichaud et al., 2000), which can result in debris flows, higher peak flow rates, poor water quality, and scouring and aggradation of the downstream channel. It has been estimated that post-fire sediment yield contributes up to 70% of the long-term sediment yield in the Colorado Front Range (Morris, 1987). These effects can degrade the hydrologic and geomorphic processes of a river system, damage aquatic habitat, and pose a threat to downstream communities (Swanson, 1981).

As the threat of wildfires continues to increase, a variety of mitigation techniques have been developed to limit post-fire runoff and sediment transport. These methods include straw mulching, forest-residue mulching, hydromulching, physical barriers, seeding, and chemical treatments. Several studies have analyzed the effectiveness of these techniques (Prats et al., 2016; Schmeer, 2018; Girona-Garcia, 2021), and one method that has proved to be a viable option at a small scale is forest residue mulching. Application of mulched wood directly to hillslopes limits surface erosion by increasing surface roughness, decreasing bare soil cover, and decreasing rainfall impact energy, which have been shown to be the three driving forces behind post-fire sediment transport (Benavides-Solorio and Macdonald, 2005; Prats et al., 2016; Foltz

and Wagenbrenner, 2010; Robichaud et al., 2010a; Wagenbrenner et al., 2006). While these studies have confirmed that, under the right conditions, mulching can limit post-fire runoff and sediment transport on the plot (10-100 m^2) to hillslope scale (100-1000 m^2), few studies have attempted to estimate the impacts of mulching at the watershed scale (> 1 km^2). Large scale aerial mulching operations are a costly endeavor; to maximize resources it is critical to understand the site-specific drivers of sediment transport, the areas at risk of contributing the most sediment, and areas where mulch can be most effective.

Large scale studies of geomorphic change have only recently become possible thanks to advancements in remote sensing and photogrammetry. In the past, studies were limited by both the spatial scale and resolution at which sediment transport data could be collected. Previous studies (e.g., Benavides-Solorio and MacDonald, 2001; Schmeer et al., 2018) relied on sediment collection via sediment fences or preconstructed plots with rainfall simulators and sediment troughs (Prats et al., 2016). More recent studies utilized light detection and ranging (LiDAR) to be able to capture geomorphic changes at a much larger scale. While LiDAR measurements could be collected on a much larger spatial scale, they were restricted by the relatively coarse spatial resolution of the datasets (Pelletier and Orem, 2014; Brogan et al., 2019). Spatial resolution is directly correlated to the threshold of changes able to be detected during processing, as spatial resolution decreases so too does the detection threshold. More recently the field has turned to Structure-from-Motion (SfM) photogrammetry techniques. SfM utilizes uncrewed aerial vehicles (UAVs), capable of collecting centimeter resolution aerial images over hundreds of acres (Ellet et al., 2019; East et al., 2021). The use of UAVs and SfM software now allows the user to detect geomorphic changes on the order of a few centimeters (Fonstad et al., 2013),

providing an invaluable tool for accurately quantifying sediment flux volumes on hillslopes and channels at much greater scales. Having an accurate assessment of the sediment budget in contributing watersheds is necessary for downstream managers to protect critical infrastructure and mitigate damaging effects to aquatic habitat.

Aerial mulching operations have been used to try to mitigate elevated levels of runoff and sediment transport. While forest residue mulching has proved effective at a small scale, large-scale aerial mulching operations are both expensive and unproven. The 2020 East Troublesome Fire in the northern Colorado Front Range provides an opportunity to investigate post-fire sedimentation and the impacts of aerial mulching at the watershed scale. The fire began on 14 October 2020 and went on to burn over 190,000 acres, making it the second largest wildfire in Colorado's recorded history. Northern Colorado Water Conservancy District, in conjunction with Grand County, the United States Forest Service (USFS), and the Bureau of Land Management (BLM) conducted aerial mulching operations over much of the burned area from June to August 2022 in an attempt to minimize sediment transport in high-risk areas. Subsequently, we have collected repeat UAV surveys of six study watershed outlets.

The goals of this study are (1) to quantify volumes of erosion and deposition for hillslopes and channels for a variety of sites at a range of elevations (2) to identify and quantify the drivers of volumetric change and their relative contributions within and across watersheds (3) to determine the impact of several near-channel parameters on sediment storage and transport within watersheds; and (4) to assess the impacts of a large-scale aerial mulching operation at scales from hillslopes to watersheds. Through these objectives we hope to better understand the roles of

site-specific characteristics on postfire sediment transport, and to better inform future mulching operations to minimize cost and maximize success.

(2) BACKGROUND AND SITE DESCRIPTION

This study focuses on a portion of the East Troublesome Fire burn scar along HWY 125, including six tributary watersheds to Willow Creek, a few miles northwest of the city of Granby. A significant portion of the study area experienced moderate to high burn severity, leading to widespread vegetation loss and ground debris, making it an ideal candidate for mulching. Two unmulched and four partially mulched areas were selected for data collection, ranging from elevations of 2,535 m to 3,619 m ASL (Figure 1). The six areas are referred to as Upper No Mulch (UNM), Upper Mulch 2 (UM2), Middle Partial Mulch (MPM), Middle Mulch (MM), Lower Partial Mulch (LPM), and Lower Mulch 2 (LM2).

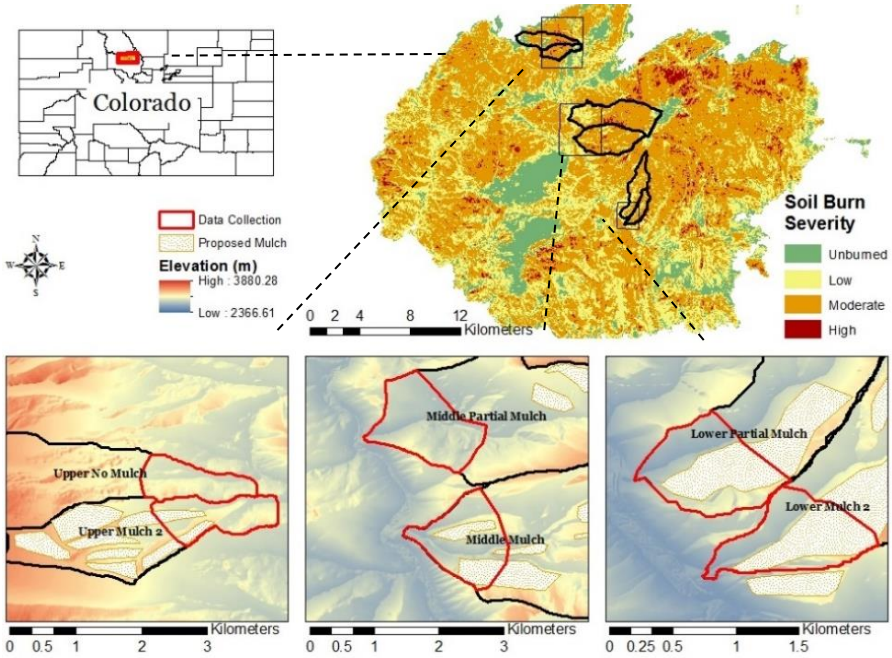

Figure 1: East Troublesome Burn area with locations of study watersheds, data collection areas (red outlines), and proposed mulching areas (white and brown hatching)

The lower and middle watershed pairs drain directly into Willow Creek, while the upper watersheds drain into Pass Creek, a tributary of Willow Creek. Each pair of watersheds share comparable geomorphic characteristics, as well as similar vegetative regrowth, precipitation

patterns, burn severity, and size (Table 1). However, these characteristics differ between the upper, middle, and lower portions of the study area (Figure 2). Mean slope was calculated from a 0.5 m pre-fire LiDAR derived DEM, burn severity percentages were calculated from Burned Area Emergency Response (BAER) maps of the area, and vegetation was calculated from RGB orthomosiacs of the study area using a semi-automatic classification algorithm. The proposed mulching areas occupied 0 to 69% of the study areas; we use these proposed areas in our analysis. Actual mulch ground coverage was likely variable over the proposed areas, but on-the-ground mulch coverage observations were not collected.

Table 1: Summary of watershed and fire metrics for each data collection area

Watershed	Area (km^2)	Mean Slope (%)	Vegetation Cover (%)	Unburned/Low Severity (%)	Moderate Severity (%)	High Severity (%)	Mulched Area (%)	Elevation range (m)
UNM	0.82	12.3	20.0	6.5	89.5	3.9	0.0	2732-2888
UM2	0.78	19.7	18.8	36.5	62.5	1.0	17.7	2654-2865
MPM	1.44	27.1	25.8	70.1	29.9	0.0	0.0	2626-2825
MM	1.19	33.8	19.3	34.3	64.9	0.8	68.5	2606-2872
LPM	0.64	39.5	27.4	67.2	32.8	0.0	45.9	2548-2812
LM2	0.61	39.6	14.0	35.1	64.9	0.0	50.1	2535-2890

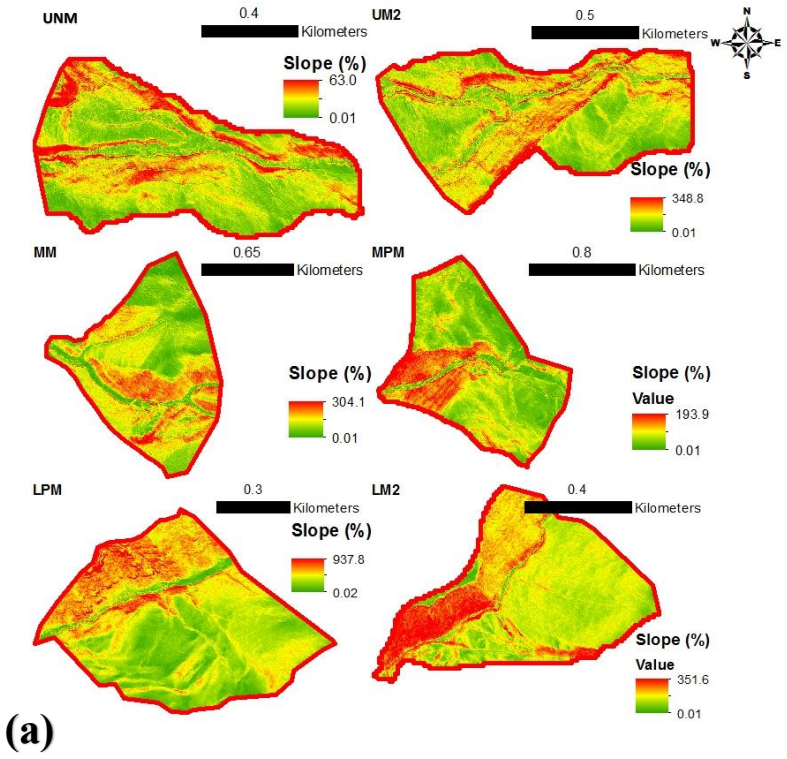

(a)

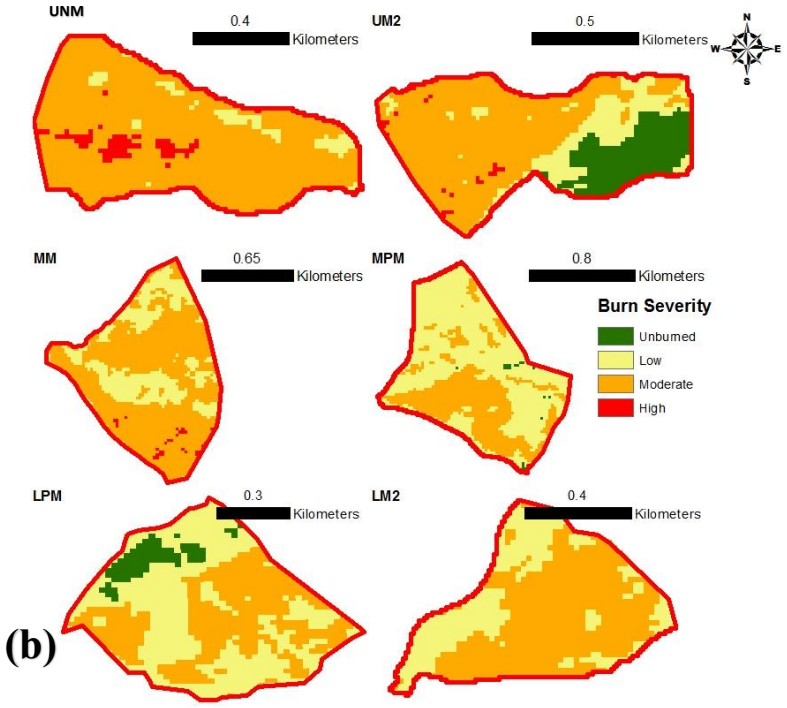

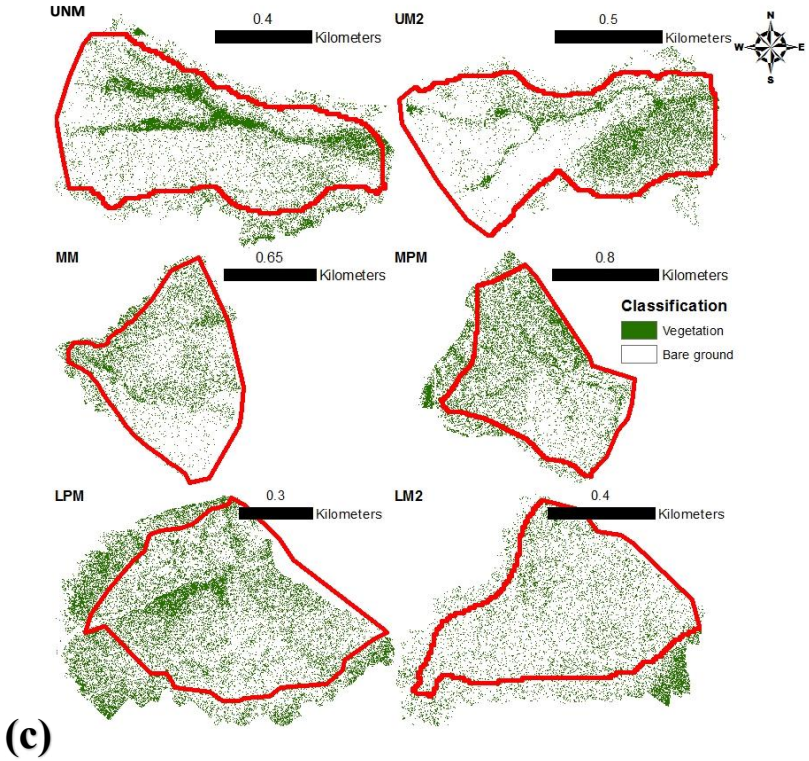

Figure 2: (a) Slope, (b) burn severity, and (c) classified vegetation in the 6 data collection areas

The study site falls within sedimentary mid-elevation and subalpine forest ecoregions, dominated by Lodgepole pine, grouse whortleberry, subalpine fir, Engelmann spruce, russet buffaloberry, and a variety of shrub and grass groundcovers (Chapman et al., 2006; Soil Survey Staff, 2023). The geology of the area includes 50% Frisco family complexes with sandstone substratum, 25% Howlett family moist complexes, derived from sandstone residuum and slope alluvium, 20% Scout family moist complexes, also derived from sandstone residuum and alluvium, with the remaining 5% consisting of a variety of minor components (Soil Survey Staff, 2023). Precipitation at the sites is extremely variable and dominated by snow in the winter and intense localized convective storms in the summer.

(3) METHODS

3.1 Drone Flights

3.1.1 Flight Planning

Aerial imagery was collected using a WingtraOne Gen II fixed wing mapping drone, operating a 42-megapixel Sony RX1R II camera payload. Flash flooding and extreme topography limited our ability to access higher portions of the watersheds, so aerial imagery was collected for areas near the watershed outlets, ranging from 0.61 to 1.44 km^2. Between July 11th and October 13th each subbasin was flown 3 times to allow for identification of erosion and deposition during that period. Mulching was completed prior to all flights, except the initial flight for UM2, which was conducted 1-2 weeks before mulching was completed in that area. One moderate rainfall event occurred between the first flight and mulching. Flight planning was conducted using Wingtra's proprietary software, WingtraHub. All flights are fully automated from take-off to landing and follow a set of input parameters specified during the planning process. For the watershed flights the drone was flown at 120 m AGL, corresponding to a ground sampling distance (GSD) of 1.6 cm per pixel, and a side and front overlap percentage of 70, which allowed for sufficient tie points to be present for SfM post-processing.

3.1.2 Flight Execution

WingtraOne is equipped with an onboard high-precision post processed kinematic (PPK) global navigation satellite system (GNSS) module. Therefore, it was not necessary to use ground control points (GCPs) to align images during post-processing (de Haas et al., 2021). WingtraOne corrects the spatial data associated with each image using a relative comparison between its raw in-flight readings and base station data collected during the flight. A Topcon GR-5 GNSS base

station unit receiver was used for this study. The receiver was set up no more than 1 km from the take-off location for the drone and collected static data at 1-second intervals for at least one hour including during the flight. The drone flights were then conducted from points high in the watershed to allow for line of sight to be maintained at all times between the pilot and the aircraft.

3.2 Post Flight Processing

3.2.1 Structure from Motion

The static data were then uploaded to the National Oceanic and Atmospheric Administration's (NOAA) Online Positioning User Service (OPUS). OPUS ties the static coordinate recorded to the National Spatial Reference System NSRS usually with an accuracy of a few centimeters, depending on location and how long the base station was recording. Our corrected accuracies ranged from 0.5 cm to 6.2 cm. Image corrections were performed using Wingtra's proprietary PPK software, WingtraHub, where each image location is corrected using the adjusted base station data retrieved from OPUS. The output from this geotagging process was an updated set of images with vertical and horizontal errors ranging from <1 to 5 cm.

These images were then processed in Agisoft Metashape structure-from-motion software. SfM processing allows the user to create three-dimensional topographic datasets from a series of two-dimensional images with associated location data. One of the major difficulties working with repeat surveys is ensuring they are aligned accurately and consistently. For this study, we followed an SfM workflow developed by the USGS (Over et al., 2021) to create dense point clouds, digital elevation models (DEMs), and orthomosaics for each flight. We were interested only in the relative differences in topography between flights, therefore we utilized a

coregistration workflow during SfM optimization (Cook and Dietze, 2019) which detects common tie points located in stable portions of the survey, minimizing relative uncertainty between the different flights. For this workflow, images from all flights of a given area were processed together in a single “chunk”, with camera locations for only one set of images being activated. The activated images were used as a reference for the other flight images during the alignment, point detection, and optimization steps. For each pair of surveys the images with the lowest reported error from the geotagging process were selected to be activated. Once optimization was completed, the images were split into individual chunks based on their flight date, and dense point clouds, DEMs, and orthomosaics were constructed and exported from Metashape.

Systematic errors that can result from GCP corrections, such as doming, were not present in any of our data sets. Therefore, error estimations could be focused on estimating precision, a measure of the random error caused by measurement uncertainty and uncertainty during SfM processing, such as tie point estimation (James et al., 2017, 2020). The errors reported from the geotagging process were imported to Metashape prior to optimization, and in conjunction with values calculated during the SfM processing, such as tie point variance, and optimization parameters, were used to calculate measurement precision of each point based on a workflow developed by (James et al., 2020). Horizontal uncertainties (0-5 mm) were significantly smaller than vertical uncertainties (1-5 cm) (Table 2), therefore they were neglected in the analysis.

Table 2: DEM resolutions and maximum and mean uncertainties for each flight

Watershed	Flight Date	DEM Resolution (cm/pix)	Max Vertical Uncertainty (cm)	Mean Vertical Uncertainty (cm)
UNM	7/18/2022	3.8	2.97	1.22
	9/8/2022	3.8	2.96	1.30
UM2	7/11/2022	3.9	3.65	1.26
	9/8/2022	4.1	3.20	1.38
MPM	9/1/2022	4.1	4.28	1.27
	10/6/2022	4.1	5.04	1.32
MM	9/1/2022	4.4	4.25	1.39
	10/6/2022	4.0	3.97	1.47
LPM	8/12/2022	4.0	3.01	1.15
	10/6/2022	4.2	3.62	1.31
LM2	8/12/2022	4.3	3.68	1.26
	10/6/2022	4.0	3.55	1.17

The vertical uncertainty values were then exported from Metashape and interpolated onto a grid with resolution equal to each DEM using kriging with a spherical semivariogram model in Surfer 13. This allowed error statistics to be calculated for each DEM (Figure 3a) and displayed as a point coordinate precision map (Figure 3b). The precision error maps were then used to calculate the detection threshold discussed in section 3.2.2.

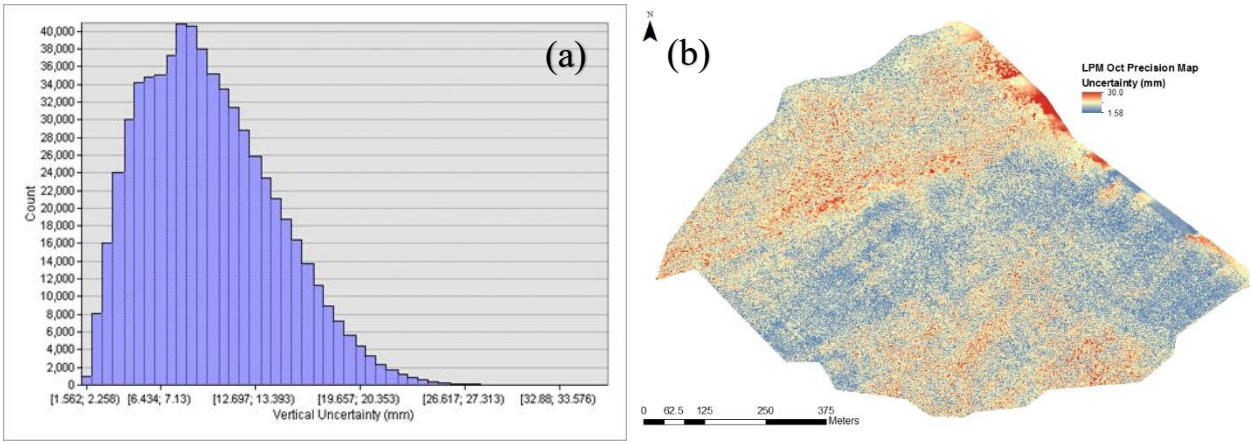

Figure 3: (a) Histogram of precision uncertainty values for LPM October DEM (b) point coordinate precision map for LPM October DEM

3.2.2 Sediment Volume

DEMs of Difference (DoDs) were calculated for each portion of the study area by subtracting the DEM of the earlier flight from the DEM of the later flight. The output from this calculation shows erosion as negative change and deposition as positive change. The next step was to filter

changes from the DoDs that fell below our calculated threshold of detection. Following the methods outlined in Dai et al. (2022), the point precision uncertainty rasters for each DEM were combined using the method developed in Anderson (2019):

$$\delta_{DoD} = \pm 1.96\sqrt{\sigma_2^2 + \sigma_1^2} \quad (1)$$

where 1.96 is the coefficient associated with a 95% confidence level from a student *t*-test, δ_{DoD} is the 95% detection threshold and σ is the point precision uncertainty for a given DEM, with subscripts 2 and 1 representing the later and earlier flights, respectively. This equation assumes no correlation between the uncertainties of the two flights.

The combined point precision map was used as a threshold of detection at each individual raster cell to filter out changes in the DoD that were within the positive and negative threshold values. This provided confidence that all changes outside of the detection threshold were occurring in the watersheds.

The sediment volumetric changes were then calculated by multiplying the filtered DoDs by the pixel area. Lastly, we calculated the uncertainty in the volumetric calculations at a 95% confidence interval (CI) using the approach of Rolstad et al. (2009):

$$\sigma_v = \sqrt{n}L^2\sigma_{DoD}\sqrt{\frac{\pi a_i^2}{5L^2}} \quad (2)$$

where σ_v is the absolute volume error, n is the number of cells in the DoD, L is the cell size, a_i is the range of the semi-variogram function, and σ_{DoD} is the standard deviation of the DoD at a 95% CI. σ_{DoD} and a_i were calculated by running a portion of the DoD through a kriging tool utilizing a spherical semi-variogram model.

3.2.3 Vegetation Filtering

After the DoDs were calculated, it was apparent that changes due to vegetation growth and decay would contribute significantly to estimated volumes, therefore, it was necessary to filter areas of vegetation out of the DoDs. Vegetation filtering was achieved using the Semi-Automatic Classification Plugin (SCP) for QGIS Desktop 3.22.7 (Congedo, 2021). SCP is a supervised classification tool, requiring the user to select a number of areas within the remote sensed data and associate them with a classification ID; in our case we created a binary classification: vegetation or non-vegetation. We used orthomosaic images, with RGB bands produced during the SfM processing phase, to perform our classification. SCP then analyzes the spectral signatures of the selected areas and classifies the entire dataset. From this a simple binary raster was created and multiplied with the DoD to set all areas with vegetation present equal to zero, effectively filtering vegetation changes out of the final change estimates. Estimates of the classification accuracy were determined using a random point sampling method which indicated the number of true-positive, true-negative, false-positive, and false-negative predictions by SCP. Points were generated at equal intervals orthogonal to the main channel; at least 100 points were sampled for each watershed. The value of the vegetation classification raster was sampled at each point and then compared with the actual groundcover, determined from the orthomosiac images.

3.2.4 In-Channel Sediment Transport Controls

From initial observations it was clear that the channels and riparian zones were especially geomorphically active, so we decided to analyze near-channel drivers of sediment transport separately from hillslope drivers. The channels were delineated to include the main channel, and near-channel areas that were inundated at least once during the study period. The channels were delineated by hand using DoDs and orthoimagery to facilitate the identification of change

resulting from channel inundation, and high-water marks. Slope (S), width (w), vegetation cover (V), stream power (S/w), change in stream power ($\Delta S/w$), and change in slope (ΔS) were identified as potential drivers of near-channel sediment transport. Stream power is traditionally calculated as the ratio of the flowrate and friction slope to the channel width; however, flowrate data was unavailable to us, so we used S divided by w as an analog for stream power. Average S and w were calculated over 10-m sampling windows that extended from the channel thalweg to the point of observable inundation during high flows. We estimated S/w as the ratio of average slope to average width over the 10 m sampling windows. Slope was calculated from a 0.5-m resolution DEM produced using prefire LiDAR flown in 2020. Prefire LiDAR was used for this instead of drone DEMs because the fineness of the drone resolution led to some very large slope values at near-vertical topography which skewed the average slope. The change in slope and stream power were calculated as the difference between the value at the upstream window and the value at the next downstream window. Longitudinal profiles of these values were then plotted alongside the thalweg profile and net channel change over the 10-m windows to facilitate identification of trends and relationships between them.

3.3 Regression Model for Drivers of Erosion and Deposition

3.3.1 Model Development

To better understand the impacts of mulching at the watershed scale it is necessary to identify local relationships between a variety of hydrologic and geomorphic drivers and sediment transport. While it has been shown that drivers such as precipitation intensity, bare soil percentage, and drainage area are directly correlated with erosion, the relationship between these characteristics can vary greatly between sites (Benavides-Solorio and Macdonald, 2005; Prats et al., 2016; Foltz and Wagenbrenner, 2010; Robichaud et al., 2010a; Wagenbrenner et al., 2006). It

is important to determine the local drivers of erosion in order to better understand the impacts of mulching.

For this study we chose to develop a bootstrap forest regression model (Breiman, 2001) capable of identifying the strength of correlation between site-specific drivers, including presence of mulch, and vertical topographic change. Bootstrap forest regression models have been shown to be particularly effective at predicting hydrologic phenomena due to their ability to handle a variety of variables with potentially non-linear or correlated relationships, their low risk of overfitting to random error in the datasets, and their effectiveness at determining the relative importance of each input variable (Eng et al., 2017; Addor et al., 2018; Miller et al., 2018). Bootstrap forest, also known as random forest, is an ensemble modeling approach that combines outputs from a large number of independent decision trees into a single model output, based on random sampling of input classifiers (Breiman, 2001).

3.3.2 Model Inputs

Four types of model setups were used to capture effects of drivers on topographic change over different spatial scales. Two models were developed for each individual subdivided watershed, one with erosion normalized by contributing area as the dependent variable, and one with deposition normalized by contributing area as the dependent variable. Two additional models were developed using combined data from all watersheds with normalized erosion and deposition as the dependent variables. We subdivided the watershed areas into hillslope and catchment scale subunits ranging from 450 m^2 to 55000 m^2, with a vast majority being between 5000 and 15000 m^2. The models developed in Kampf et al. (2020) performed well using catchments in this size range. Delineations were created using ESRI ArcHydro delineation Tools in Arcmap 10.8.1. This method allowed us

to view watershed-scale processes as a culmination of site-specific relationships at a smaller scale. In each case the erosion and deposition volumes were normalized by dividing them by the sub-unit area. We then log-transformed the normalized deposition volumes, and the absolute value of the normalized erosion volumes, to achieve a more normal distribution of the datasets.

Precipitation totals and intensities were estimated using NOAA Multi-Radar Multi-Sensor (Zhang et al., 2016) Quantitative Precipitation Estimates (MRMS QPEs) and compared with local rain gauges to verify accuracy. Radar-only QPE is corrected using the Multisensor 1-hour QPE, at which point the correction bias is used to resample the precipitation estimates to 1-min accumulations for 1 km^2 grid cells using a Python script. The calculated 1-min accumulations were then used to calculate the daily accumulations and compare the estimated 15-min intensity with the on-site gauge. Because this region experiences brief, localized, intense convective storms, it is difficult to estimate spatial patterns of precipitation at spatial scales below 1 km^2 and therefore verification was conducted to ensure that accumulations were occurring at similar times and with comparable peak values. Wilson et al. (2018) identified the 60-minute maximum intensity to be successful at separating precipitation events that generated sediment transport from those that did not. Once we were satisfied that the MRMS estimates were adequate, the daily accumulations were summed over the period between the first and last data collection date, and 60-min maximum intensities were calculated for 1 km^2 grid cells. The grid was then overlayed the study area where the values corresponding to each subunit were exported.

We then built the model in JMP, a statistical analysis software, using an 80% training, 20% testing data split. Prior to running the model, input variables were analyzed for collinearity within JMP,

to determine a set of parameters that were not significantly correlated with one another ($r < 0.85$). All model setups were run using the same independent predictor variables for each subunit, including, mean slope (*S*), hillslope length (*L*), mean width (*w*), maximum 60-minute precipitation intensity (*MI60*), total precipitation accumulation (*P*), mean differenced normalized burn ratio (*dNBR*), bare ground coverage, defined as areas absent of vegetation (*BG*), and mulch coverage (*M*). Mulch coverage values were calculated as the percent overlap between the proposed mulching areas and each subbasin. Bare ground percentages include any areas not classified as vegetation, including, bare soil, rock outcrops, ground litter, downed trees, and open water. Models were also run including vertical uncertainty as one of the independent variables to ensure it was not significantly correlated with topographic change.

The dependent variables of log-transformed normalized erosion and deposition volumes reflect topographic differences between surveys, which were conducted at different times during the season for the different watersheds (Table 2). This may have an impact on the statistical analysis, but we aimed to minimize potential complications by computing the time-dependent precipitation variables (*MI60* and *P*) using data from the time between the two flights for each watershed, so that measured erosion and deposition only reflect precipitation events that occurred during the observation period for each watershed.

Model performance was assessed using both the coefficient of determination, R^2, and root mean squared error (RMSE). Because the model relies on random sampling, we ran both models 25 times for each watershed to ensure sufficient input data coverage, and identified the model runs with the highest performance metrics. The five model runs with the best performance metrics

were then compared with the predictions of all the model runs to determine the result that was most accurate and representative of the natural phenomena. This was achieved by determining the most common ranking for each predictor and choosing the model from the five most accurate that was most representative of this modal ranking. This helped to avoid choosing an anomalous model run that was not representative of the overall model performance.

(4) RESULTS

4.1 Precipitation

MRMS estimates of 60-min maximum intensity and total accumulation were first compared with USGS gauge 401642106051601 and an on-site tipping bucket rain gauge located at 40.249418 N, 106.083132 W, roughly 2 km from the outlets of MPM and MM. Table 3 shows comparisons between the two local gauges and the MRMS estimates for each watershed. The gauges only provide data at a single point, so there is no maximum or minimum *P*, the value just represents the total accumulation at those points. Since MRMS provides spatially variable precipitation, the maximum and minimum *P* indicate the largest and smallest total accumulations experienced by a portion of the watershed, respectively. The similarity of the values gave us confidence that the MRMS data is representative of the conditions occurring at the sites. Each date range was checked for the local gauges and was found to be within a few centimeters of the MRMS estimates.

Table 3: Rain gauge data compared with MRMS estimates for rain events between flights

Source		MI60 (mm/hr)	Max P (mm)	Min P (mm)
Local (date range)	USGS (7/1-10/1)	17	133	-
	Tipping Bucket (6/20-10/18)	13	128	-
MRMS (date range)	LM2 (8/12-10/6)	7	48	48
	LPM (8/12-10/6)	7	48	46
	MM (9/1-10/6)	5	23	22
	MPM (9/1-10/6)	6	27	24
	UNM (7/18-9/8)	12	124	119
	UM2 (7/11-9/8)	15	124	117

Figure 4 shows a few examples of the comparisons between the MRMS 15-min intensity and the 15-min intensity at the tipping bucket gauge. It is apparent that the MRMS does not replicate the actual rainfall exactly, but it is successful at estimating the time and magnitude of precipitation relatively accurately.

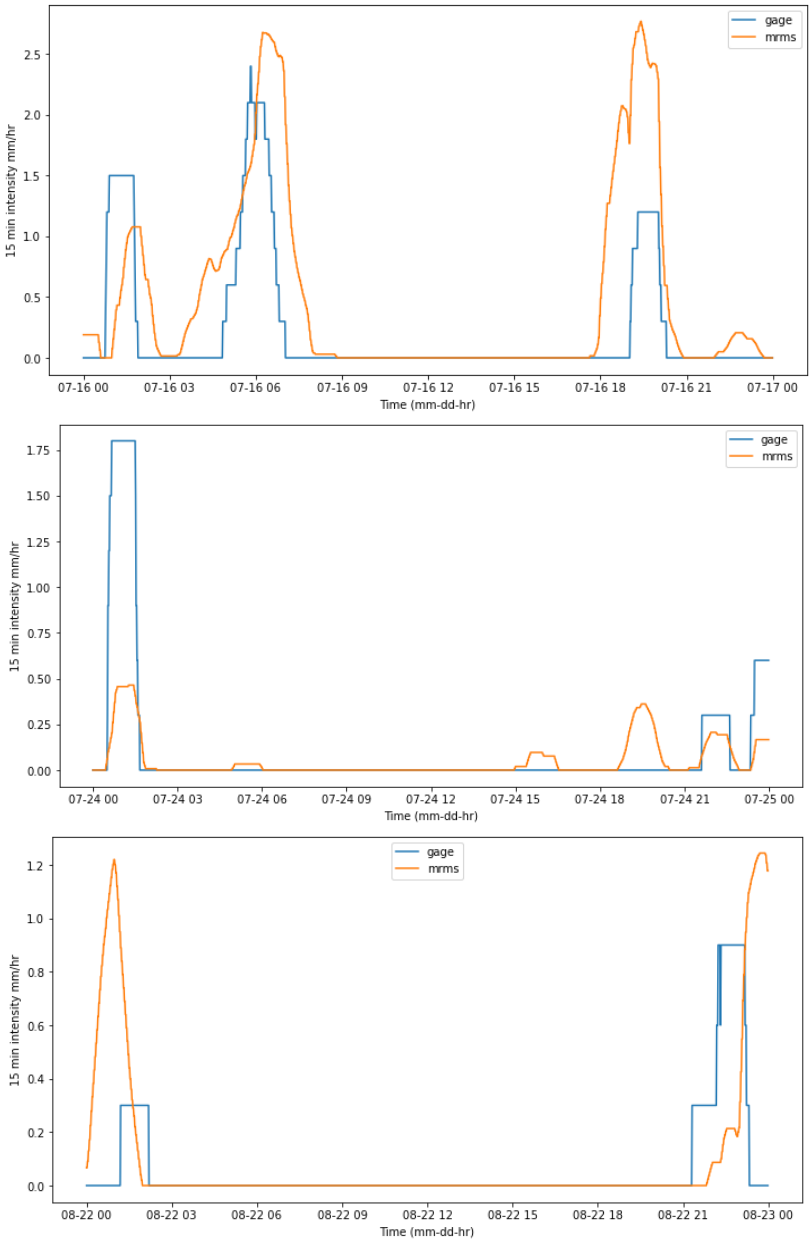

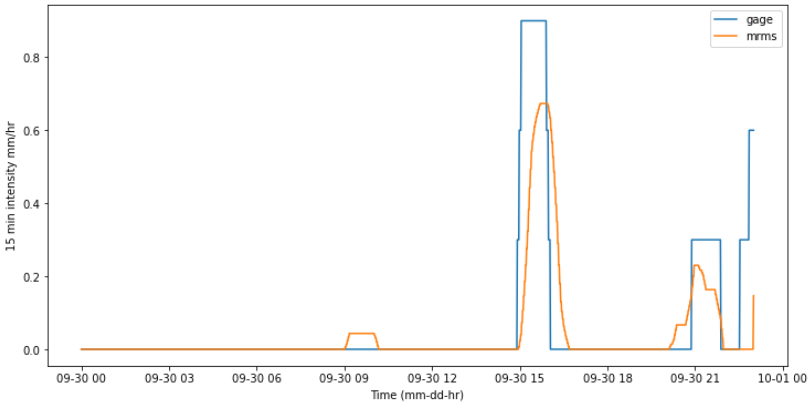

Figure 4: MRMS simulated 15-minute intensity compared with on-site tipping bucket rain gauge

Due to the coarse spatial resolution of the MRMS data there is low variability of the intensities and total accumulations within each watershed and pairs of watersheds. There was, however, significant variability across the upper, middle, and lower portions of the study area. Precipitation values were greatest during the earlier data collection periods, with the most precipitation falling during the upper watershed's data collection period, followed by the lower pair, and lastly the middle pair having the lowest total accumulation. 60-minute intensities also followed a similar pattern, with summer storms weakening as the study period moved into fall.

4.2 Topographic Change and Detection

Spatial patterns of erosion and deposition varied greatly across the six study watersheds. Rilling and gully formation were prevalent on hillslopes for both LPM and LM2 (Figure 5a), with vertical changes up to 60 cm in some locations. The remaining watersheds exhibited little to no signs of rilling or gulley formation. Alternating areas of erosion and deposition occurred along the near-channel portions of each watershed (Figure 5b). Channel erosion in LPM, LM2, and MM appeared to be a result of aggressive head cutting of mobile bank sediment, which is enhanced by the high degree of confinement of those channels. MPM and the upper watersheds were better protected by vegetation and had better floodplain connectivity, which led to less extreme channel changes in these watersheds.

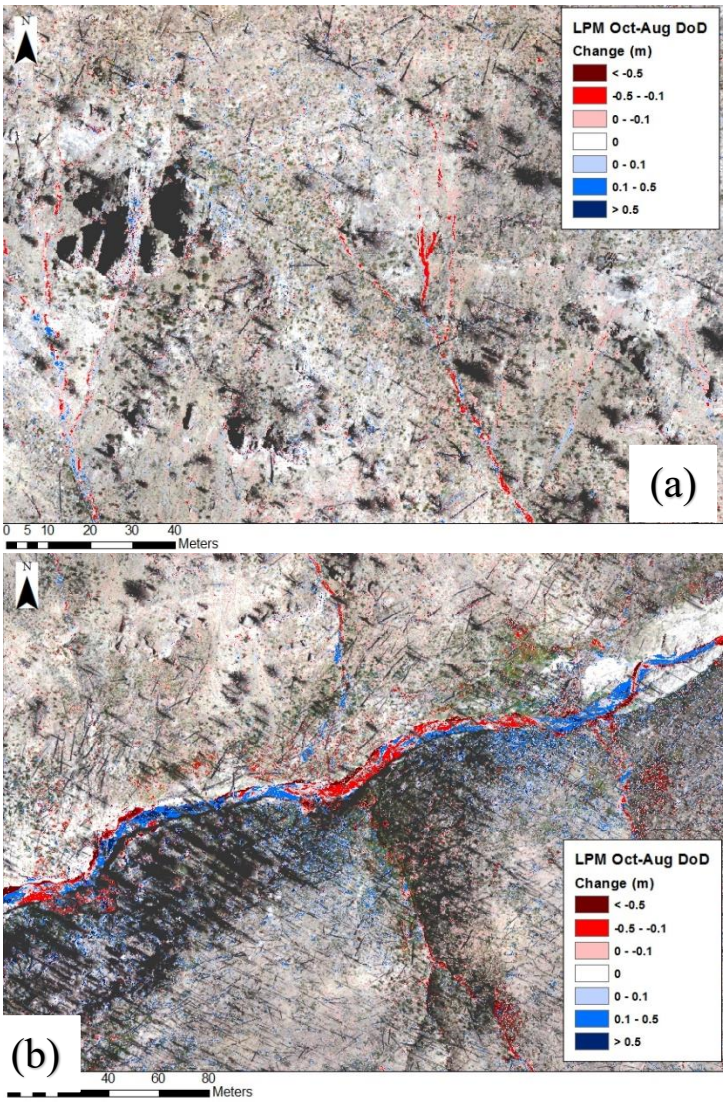

Figure 5: (a) Hillslope rilling and gulley formation in LPM, (b) near-channel erosion and deposition in LPM, red indicates erosion and blue deposition

The level of detection for each raster cell was specified as the maximum vertical uncertainty at the point (Equation 1); the maximum and mean uncertainties for each DEM and DoD can be seen below (Table 4). Vertical uncertainties were not randomly dispersed over the study area. With few exceptions, the highest uncertainties occurred in locations with dense vegetation, and along the valley floors (Figure 6).

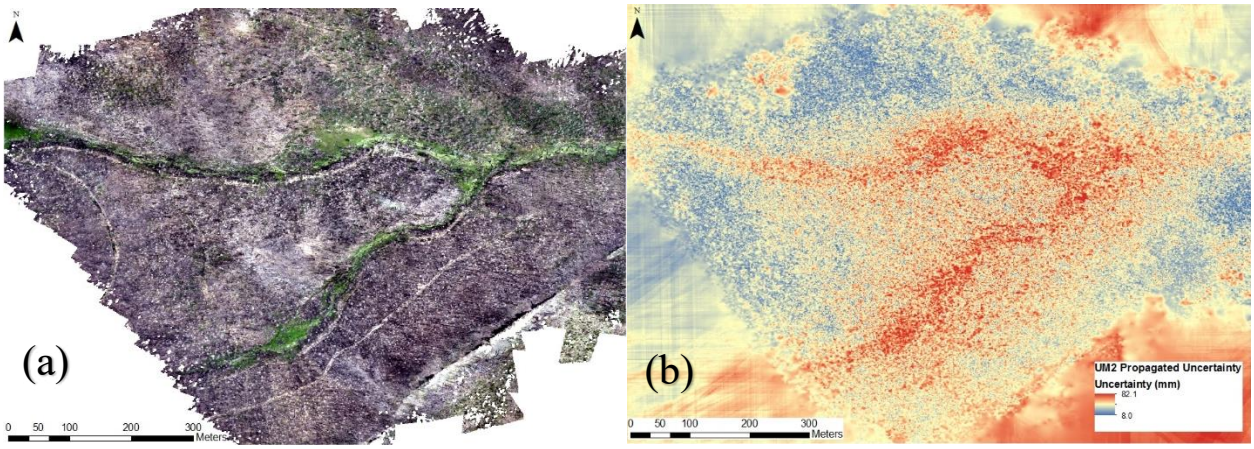

Figure 6: (a) UM2 orthomosaic displaying areas with dense vegetation along the stream corridor (b) propagated uncertainty map for UM2 showing higher uncertainty values in vegetated areas

SfM processing often has difficulty identifying common tie points in areas with vegetation, shadowing, and standing water (Dai et al., 2022), therefore it is reasonable to expect relatively higher uncertainties at these locations.

Table 4: Propagated vertical uncertainties at 95% confidence level for the six study sites

Watershed	Flight Date	Max Propagated Uncertainty 95% CI (cm)	Mean Propagated Uncertainty 95% CI (cm)
UNM	7/18/2022 9/8/2022	7.33	3.5
UM2	7/11/2022 9/8/2022	8.21	3.68
MPM	9/1/2022 10/6/2022	10.92	3.61
MM	9/1/2022 10/6/2022	9.76	3.99
LPM	8/12/2022 10/6/2022	7.58	3.41
LM2	8/12/2022 10/6/2022	9.03	3.38

4.3 Vegetation Filtering

The reliability of the vegetation filtering was inconsistent, and the method noticeably struggled with very bright and very dark areas of the orthomosaics. This led to uneven filtering in LM2, LPM, and UNM (Figures 7 a, b), and generally unsuccessful filtering in UM2, MM, and MPM (Figures 7 c, d). Significant volumes of detected change were removed via filtering for each

watershed but the volumes for UM2, MM, and MPM were negligible compared to the actual volume changes contributed by vegetation growth and decay.

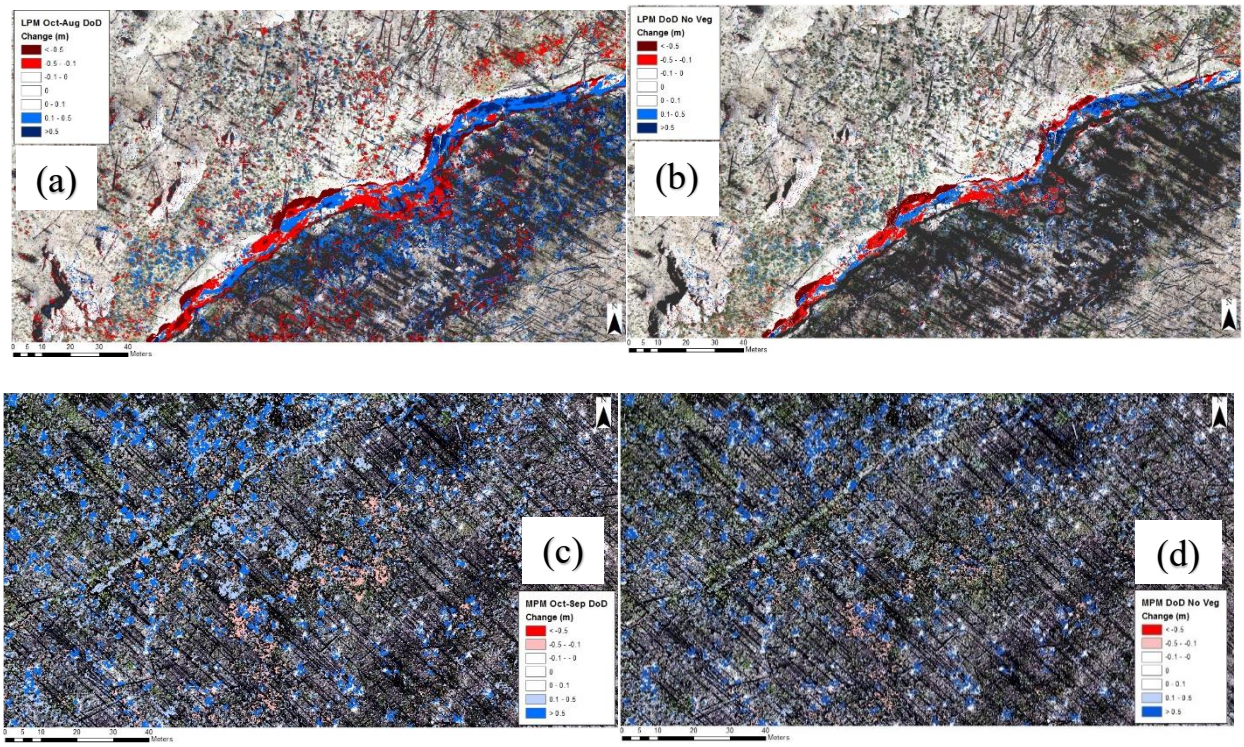

Figure 7: (a) LPM unfiltered DoD, showing large magnitudes of change in vegetated areas (b) LPM DoD after vegetation filtering, showing generally successful removal of vegetation (c) MPM unfiltered DoD, showing large depositional magnitudes from vegetation (d) MPM DoD after vegetation filtering, showing insufficient removal of changes due to vegetation

Most changes due to vegetation in MM and MPM appeared as deposition, while large erosional values occurred at treetops in UM2. Changes greater than 2 m were filtered out of UM2 to reduce vegetation effects on volume estimates, and analysis of MM and MPM was limited to hillslope erosion, and channel changes only.

Table 5 shows the results of the random point sampling, with true-positive indicating correctly predicted vegetation, true-negative indicating correctly predicted bare ground, false-positive representing incorrectly identified vegetation, and false-negative incorrectly identified bare

ground. Higher FP values indicate the classification algorithm is overpredicting presence of vegetation, while higher FN values signify underestimation of vegetation. MM, MPM, and UM2 had the poorest filtering results.

Table 5: Point sampling results showing number of true-positive (TP), true-negative (TN), false-positive (FP), and false-negative (FN) predictions for each watershed

WS	TP	TN	FP	FN	Correct %
UNM	16	75	7	9	85
UM2	10	71	15	10	76
MPM	13	48	11	31	59
MM	11	64	11	18	72
LPM	25	108	19	15	80
LM2	8	83	6	14	82

4.4 Volumes of Watershed-Scale Erosion and Deposition

MPM and UNM had no mulch coverage, UM2 had the lowest mulched area, 17.7%, with the other three having mulched areas ranging from 46-69%. Erosion volumes were greatest in the upper watersheds (Table 6), while MM, MPM, LPM, and LM2 experienced comparable normalized erosion depths between 4.7 and 6.1 mm (Table 7). Both lower basins were net depositional, which can likely be attributed to sediment being transported from higher in the watershed and deposited at the watershed outlet or along the channel where slopes decrease, and/or width increases. LM2 retained the most sediment with an excess of 1,500 cubic meters being deposited. UNM and UM2 were both net erosional, with UNM losing the most, roughly 2,500 cubic meters of sediment, over the study period.

Table 6: Calculated volumes of erosion and deposition with uncertainties at 95% CI for watersheds and channels

Watershed	Net Change (m^3)	Total Erosion (m^3)	Total Deposition (m^3)	Hillslope Erosion (m^3)	Hillslope Deposition (m^3)	Channel Erosion (m^3)	Channel Deposition (m^3)
UNM	-2508 (±1214)	-7556 (±367)	5048 (±327)	-7219 (±367)	4717 (±321)	-337 (±10)	331 (±75)
UM2	-1422 (±653)	-4941 (±208)	3519 (±176)	-4839 (±206)	3284 (±170)	-102 (±503)	235 (±864)
MPM	-	-8834 (±1639)	-	-8607 (±1639)	-	-227 (±38)	149 (±92)
MM	-	-5957 (±1116)	-	-5410 (±1112)	-	-547 (±183)	1815 (±511)
LPM	310 (±1236)	-3025 (±343)	3335 (± 432)	-1692 (±343)	2847 (±423)	-1333 (±19)	488 (±373)
LM2	1572 (±238)	-3220 (±68)	4792 (± 77)	-2812 (±68)	4108 (±76)	-408 (±6)	684 (±37)

Table 7: Total, hillslope, and channel erosion and deposition volumes normalized by contributing area

Watershed	Net/Area (mm)	Erosion/Area (mm)	Deposition/Area (mm)	Hillslope Ero/Area (mm)	Hillslope Dep/Area (mm)	Channel Ero/Area (mm)	Channel Dep/Area (mm)
UNM	-3.2	-9.2	6.2	-9.6	6.3	-11.6	11.4
UM2	-1.9	-8.5	6.0	-6.7	4.5	-9.8	22.5
MPM	-	-6.1	-	-6.5	-	-17.3	11.4
MM	-	-5.0	-	-5.0	-	-18.1	59.9
LPM	0.6	-4.7	5.2	-3.2	5.3	-115.2	42.2
LM2	3.0	-5.3	7.9	-5.5	8.0	-33.0	55.4

Figure 8 below shows erosion and deposition volumes in mulched and unmulched portions of the study areas. Erosion per area is lower in mulched areas than in unmulched areas in the upper and lower watershed pairs, and larger in MM. MPM and UNM had no mulch coverage, and deposition volumes for MPM and MM could not be trusted due to excess vegetation, thus no changes are shown for these scenarios. Deposition rates were similar for mulched and unmulched areas, with mulched deposition per area being slightly higher in UNM and LPM, and slightly lower in UM2 and LM2.

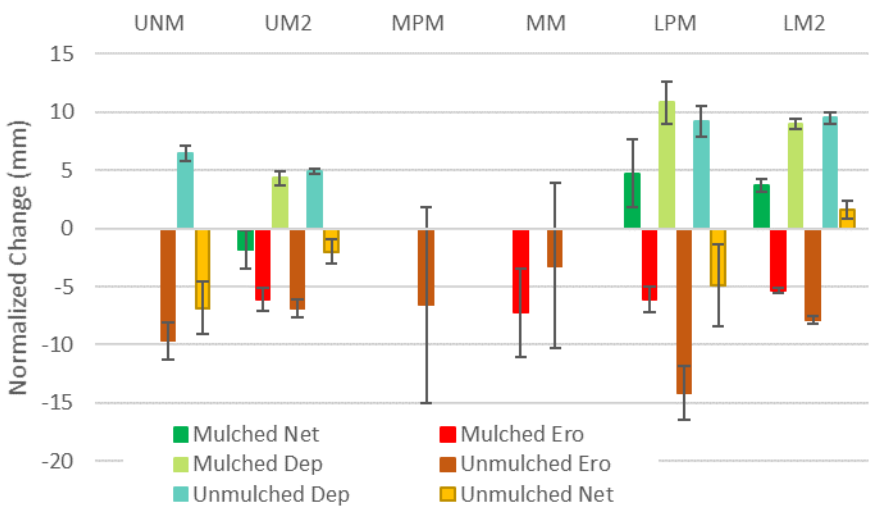

Figure 8: Normalized volumes of erosion and deposition for six watershed outlets subdivided by presence of mulch, with error bars representing uncertainty in the volumes at a 95% CI

Channel dynamics were quite varied with channel contributions ranging from <1% to 44% of total erosion volume, and 6-15% of depositional volume. Channels demonstrated higher levels of erosion and deposition per area than hillslopes in all six study sites, with the lower watersheds experiencing 3-10 times the levels of the others (Figure 9). MM channel was net depositional, LPM was net erosional, and the remaining channels were relatively close to equilibrium. See section 4.6 for more detailed results regarding channel dynamics.

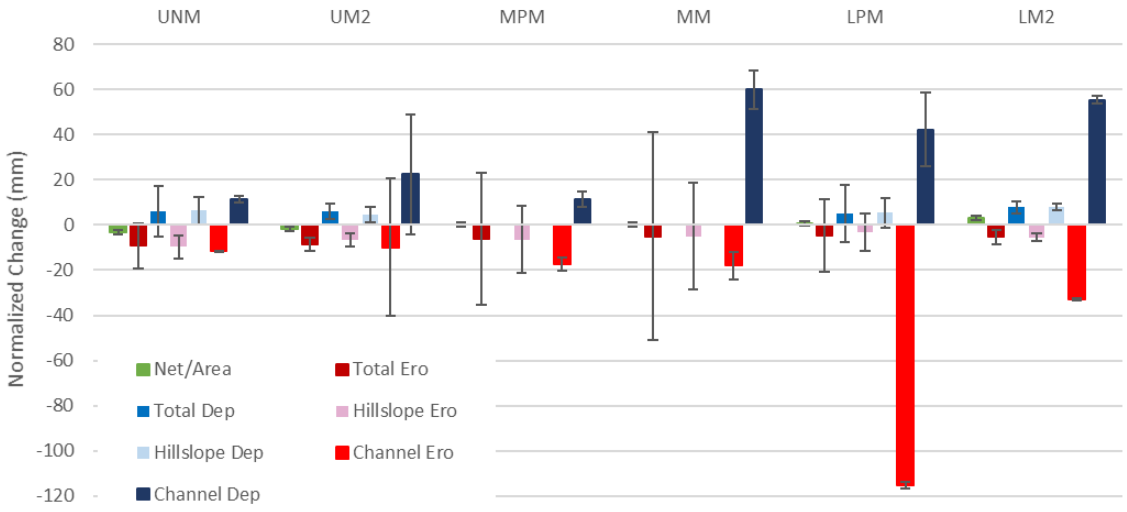

Figure 9: Erosion and deposition normalized by area for the six study locations divided by total, hillslope, and channel areas, error bars represent the uncertainty in the volume calculations at a 95 % CI

4.5 Watershed-Scale Erosion Controls

Performance of the bootstrap regression models was generally good, with R^2 values ranging from 0.53 to 0.85 and RMSE values ranging from 0.30 to 0.72 m. The performance of the testing datsasets were consistently poorer than the training dataset, with R^2 and RMSE ranges of 0.00 to 0.75 and 0.34 to 0.80 m, respectively. The model runs including uncertainty as an independent variable indicated that it was not significantly correlated with erosion or deposition, with contribution values falling below 5%. Model outputs included Pearson correlation coefficient matrices (Figure 10), relative parameter contributions (Figure 10), and partial dependence plots (Figures 11, 12). Correlation coefficients, parameter contributions, and partial dependence plots for model runs not displayed in the text can be found in the Appendix.

Combined	log(Ero/A)	log(Dep/A)	w	L	S	MI60	P	dNBR	BG	M
log(Ero/A)	1.000	0.001	0.032	-0.107	0.000	-0.234	0.292	-0.128	-0.227	-0.149
log(Dep/A)	0.001	1.000	0.099	0.074	0.286	0.514	-0.265	-0.152	-0.157	0.045
w	0.032	0.099	1.000	0.072	-0.075	0.089	0.080	-0.060	-0.066	-0.186
L	-0.107	0.074	0.072	1.000	0.027	0.122	-0.160	0.028	0.221	0.182
S	0.000	0.286	-0.075	0.027	1.000	0.077	-0.648	-0.179	-0.076	0.191
MI60	-0.234	0.514	0.089	0.122	0.077	1.000	-0.149	0.002	0.143	-0.031
P	0.292	-0.265	0.080	-0.160	-0.648	-0.149	1.000	0.225	0.123	-0.394
dNBR	-0.128	-0.152	-0.060	0.028	-0.179	0.002	0.225	1.000	0.439	0.397
BG	-0.227	-0.157	-0.066	0.221	-0.076	0.143	0.123	0.439	1.000	0.214
M	-0.149	0.045	-0.186	0.182	0.191	-0.031	-0.394	0.397	0.214	1.000

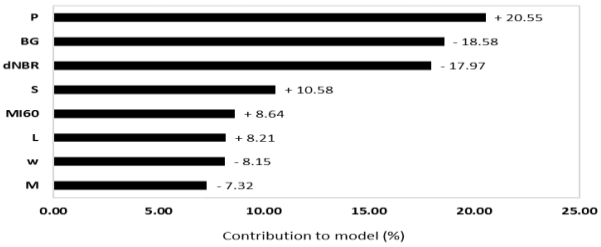

Figure 10: (Left) Pearson correlation coefficients for combined erosion model (Right) relative contributions of each parameter to combined erosion; values indicate percent contribution and signs indicate positive or negative relationship with erosion

Table 8 shows the results from the top performing model run for each set-up, emphasizing the complex and dynamic relationships between site-specific conditions and geomorphic change.

Table 8: Contribution rankings for each model set-up including positive or negative Pearson correlation coefficient

	Deposition							Erosion						
Watershed	UNM	UM2	MPM	MM	LPM	LM2	Combined	UNM	UM2	MPM	MM	LPM	LM2	Combined
R^2	0.622	0.845	-	-	0.529	0.640	0.829	0.787	0.815	0.641	0.620	0.618	0.799	0.779
RMSE	0.416	0.409	-	-	0.693	0.297	0.452	0.430	0.380	0.303	0.548	0.721	0.320	0.457
Most	BG (-)	BG (-)	-	-	L (-)	S (+)	P (-)	BG (-)	BG (-)	BG (+)	S (+)	S (+)	S (+)	P (+)
2	L (+)	MI60 (-)	-	-	M (+)	L (-)	BG (-)	dNBR (-)	dNBR (-)	S (+)	M (+)	dNBR (-)	L (-)	BG (-)
3	dNBR (-)	P (+)	-	-	S (+)	M (-)	S (-)	L (-)	L (+)	dNBR (-)	w (-)	BG (-)	M (-)	dNBR (-)
4	S (-)	dNBR (-)		-	w (+)	dNBR (+)	dNBR (+)	w (+)	S (-)	L (+)	BG (+)	L (+)	BG (-)	S (+)
5	w (+)	L (-)	-	-	dNBR (+)	BG (-)	MI60 (+)	S (+)	MI60 (-)	w (-)	L (-)	M (+)	w (-)	MI60 (+)
6	MI60 (-)	w (-)	-	-	BG (-)	w (+)	L (+)	MI60 (-)	P (-)	MI60 (+)	dNBR (+)	MI60 (-)	dNBR (+)	L (+)
7	P (-)	S (-)	-	-	P (+)	P (-)	w (-)	P (-)	w (-)	P (-)	MI60 (-)	w(-)	P (-)	w (-)
Least	M (N/A)	M (-)	-	-	MI60 (+)	MI60 (+)	M (-)	M (N/A)	M (-)	M (N/A)	P (-)	P (-)	MI60 (+)	M (-)

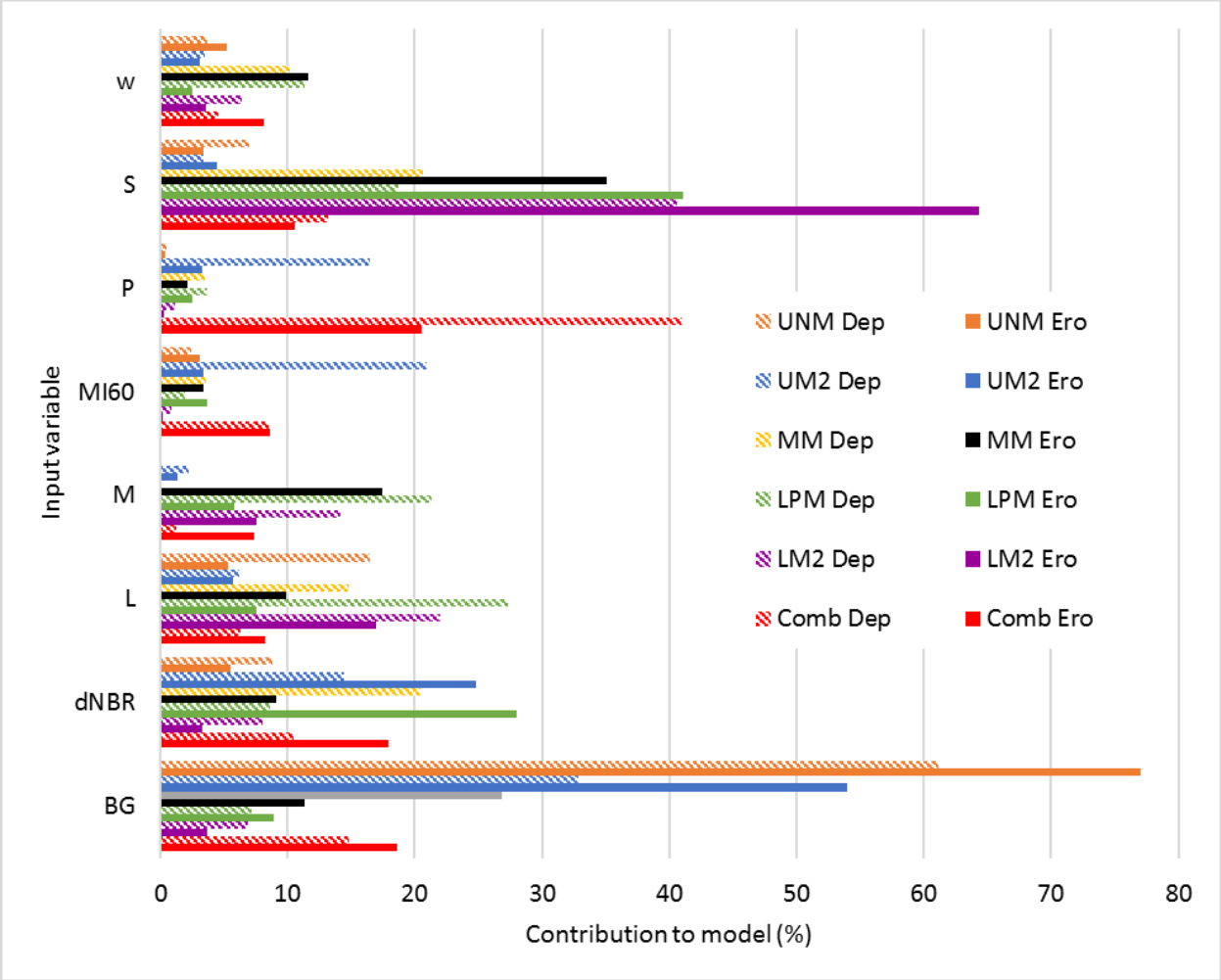

Figure 11: Magnitudes of model contributions for input variables of each model run

4.5.1 Individual erosion models

Mean slope (*S*) is indicated as contributing most to erosion in MM, LPM and LM2, and second most in MPM, which coincidentally have the four highest average slopes. *S* is indicated to have a positive correlation with erosion in all watersheds except for UM2. Area absent of vegetation (*BG*) is the strongest contributor to erosion in UNM and UM2 but is negatively correlated. In fact, *BG* is negatively correlated with erosion in all model runs except for MM and MPM. Length (*L*) and mean *dNBR* are the remaining drivers that consistently contributed greater than 10% to erosion. *L* displayed a nonlinear relationship in all watersheds. In several models, the partial dependence plots show a positive correlation between *L* and erosion for lengths less than

250 m, and a negative correlation for longer slopes (Appendix Figures 10, 12, 15, and 16). *dNBR* was also inconsistent across the study sites, showing either negative correlations or negative followed by positive for values above 400 (Appendix Figures 10, 15 and 17). *dNBR* values ranging from 300-550 are classified as moderate severity, with values larger than 550 indicating high burn severity. Width (w*),* precipitation accumulation (*P*), and 60-minute max intensity (*MI60*) all contributed negligibly to erosion across the six watersheds. Mulch was an inconsistent contributor to the models with a strong positive correlation with erosion in MM, a weak positive correlation in LPM, and the others weakly negatively correlated.

4.5.2 Combined erosion model

The combined model, which included data from all six study sites, produced very different results than the individual model runs. Primarily, *P* and *MI60* went from being negligible contributors to contributing the most and fifth most to erosion, respectively. *BG* is found to be negatively correlated to erosion, and contributes almost as much as *P*, around 20%. Similar to the individual model runs, *dNBR* showed a negative correlation with erosion for *dNBR* values under 400 and a positive correlation with erosion for values greater than 400 (Figure 12). *S* also contributed over 10% to the model and demonstrated a positive relationship between slope and erosion (Figure 12). *L* was a small contributor and showed a negative correlation for lengths less than 300 m and a small positive correlation for slopes longer than 300 m.

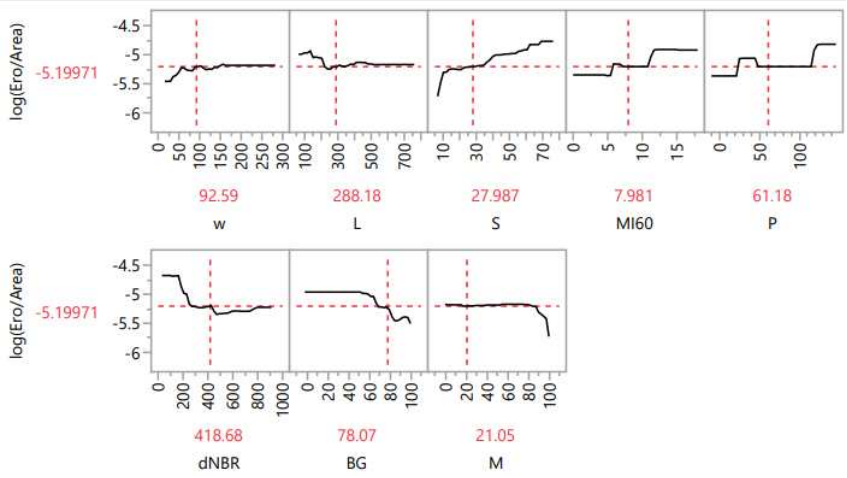

Figure 12: Partial dependence plots for the combined erosion model.

4.5.3 Individual deposition models

Model runs for deposition were not conducted for MM and MPM due to insufficient vegetation filtering. The main drivers of deposition were variable across the individual model runs and the combined model. *BG* was the dominant driver in the upper pair, one of the smallest contributors in the lower pair, and was negatively correlated with deposition in all 4 sites. *L* was a moderate contributor in all four watersheds, displaying a negative relationship for lengths less than 300 m and positive for longer lengths in several cases (Appendix Figures 11 and 13). *S* was the biggest contributor in LM2 and third largest in LPM with strong positive correlations for slopes less than 40 percent and a small negative correlation for slopes greater than 40 percent (Appendix Figures 17 and 19). *M* had a strong positive correlation with deposition in LPM, and weak correlations in the other two sites. *P* and *MI60* had considerable contributions in UM2, where deposition was negatively correlated with *MI60* and positively correlated with *P*. Lastly, *dNBR* contributed moderately across the 4 individual models, with negative correlations in the upper watersheds and positive correlations in the lower sites.

4.5.4 Combined deposition model

The combined deposition model was dominated by *P*, with *BG*, *S*, and *dNBR* all contributing above 10%. *P* had a strong negative correlation with deposition (Figure 13). *BG* also had a strong negative correlation with deposition, with deposition decreasing sharply for *BG* percentages greater than 60%. *S* was the third highest contributor with slopes below 30% being positively correlated with deposition and slopes larger than 30% being negatively correlated. *MI60* displayed a positive correlation for the low and high intensities and a negative correlation for the moderate intensities (Figure 13). *dNBR* had a moderate contribution at around 11% and had a weak correlation as burn severity increased. *L*, *w*, and *M* had little contribution and weak correlations to deposition.

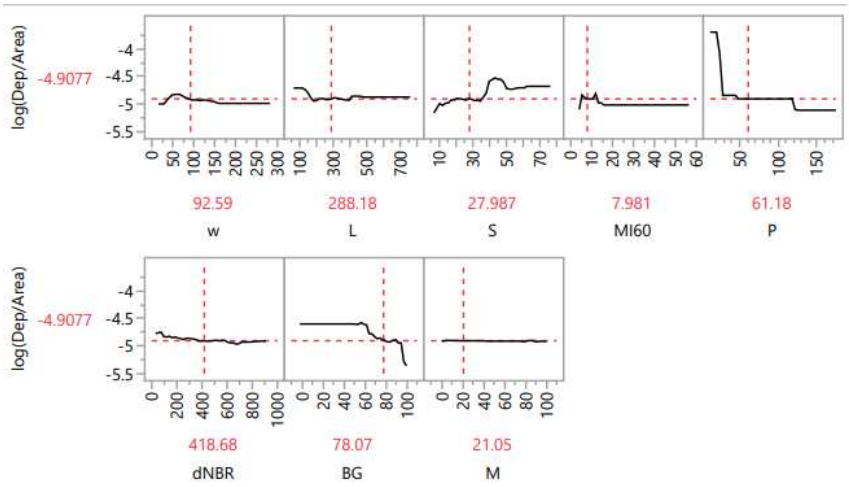

Figure 13: Partial dependence plots for combined deposition model

4.6 Channel Erosion and Deposition

Appendix Figures 31-39 show longitudinal profiles, from top to bottom, of elevation (*Z*), normalized net channel change over 10 m windows (Vol/Area), slope (*S*), change in slope (ΔS), mean width of the 10 m windows (*w*), stream power (*S*/*w*), change in stream power ($\Delta(S/w)$), and bare ground percentage within the windows (*BG*), respectively. Areas where the relationship

between these parameters is clear are shown below in Figures 14-21. Included with the six main channel sections are three tributaries, from UNM, UM2, and MM, that share similar characteristics to the main channels. MPM and LPM were net erosional, LM2, MM, and UM2 were net depositional, and UNM had essentially no net loss or storage. The tributaries were all net depositional. It is important to understand near-channel sediment dynamics as channels can be a significant mechanism in watershed scale sediment flux. For example, channel erosion in LPM was responsible for over a third of the total erosion volume in that watershed. When normalized by channel area, LPM, LM2, and MM were by far the most dynamic for both erosion and deposition.

It is unlikely that there will be one dominant driver of channel change; instead, a complex and varying relationship between site-specific characteristics will result in different levels of channel change. Figures 14-21 provide evidence of these complex relationships and shed some light onto what combination of characteristics can result in transport or storage. LM2 and LPM channels were characterized by high degrees of confinement, with unstable banks, and large volumes of transportable sediment. This resulted in consistently narrow channel widths, and high percentages of BG. Therefore, increasing S and S/w proved to be the driving factors behind erosion (Figure 14). Deposition was influenced by all factors, with increasing *w*, decreasing *S* and *S*/*w*, and decreasing *BG* all contributing to areas of deposition (Figure 15). The middle pair were relatively less dynamic but identifiable trends were apparent. Erosion in MM and MPM was heavily dependent on the relationship between *w* and *BG*. Erosion occurred at constrictions with increasing *S*/*w*, as well as at widenings where *BG* was increasing (Figures 16-18). The drivers of deposition were less clear, displaying a complex relationship between the parameters

and additional site characteristics. The largest depositional area in MPM Appendix Figure 36 appeared to be a result of a culvert at a road crossing which likely backed up high flows, dissipating energy, and allowing sediment to settle in the surrounding areas. The near-channel area in the upper pair of watersheds was characterized by dense grass and groundcover. This led to these channels having the lowest *BG* and high volumetric uncertainties. Despite this, there were clear signals that all parameters contributed to erosion and deposition in the watersheds. Areas with increasing *w*, decreasing *S*/*w*, and decreasing *BG* displayed significant deposition (Figures 19-21). Conversely, erosion occurred at locations with increasing *BG*, and decreasing *w* and *S*/*w*.

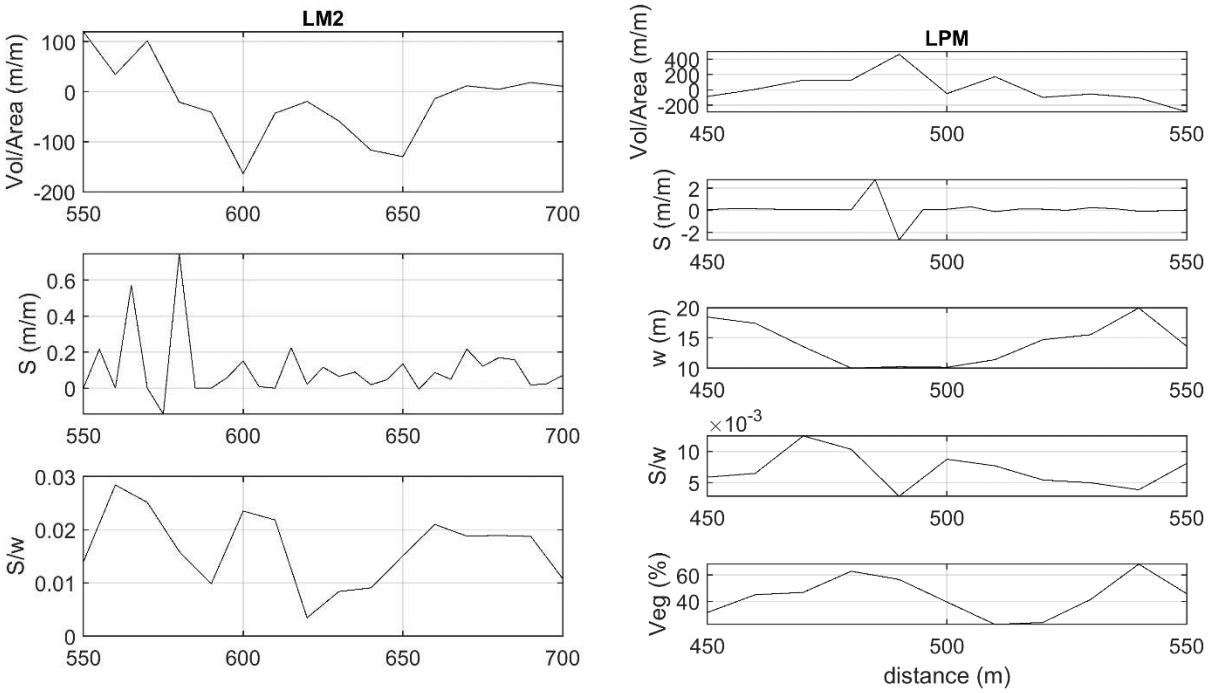

Figures 14 (Left) and 15 (Right): Longitudinal profiles of near-channel characteristics in areas of interest in LM2 and LPM, respectively

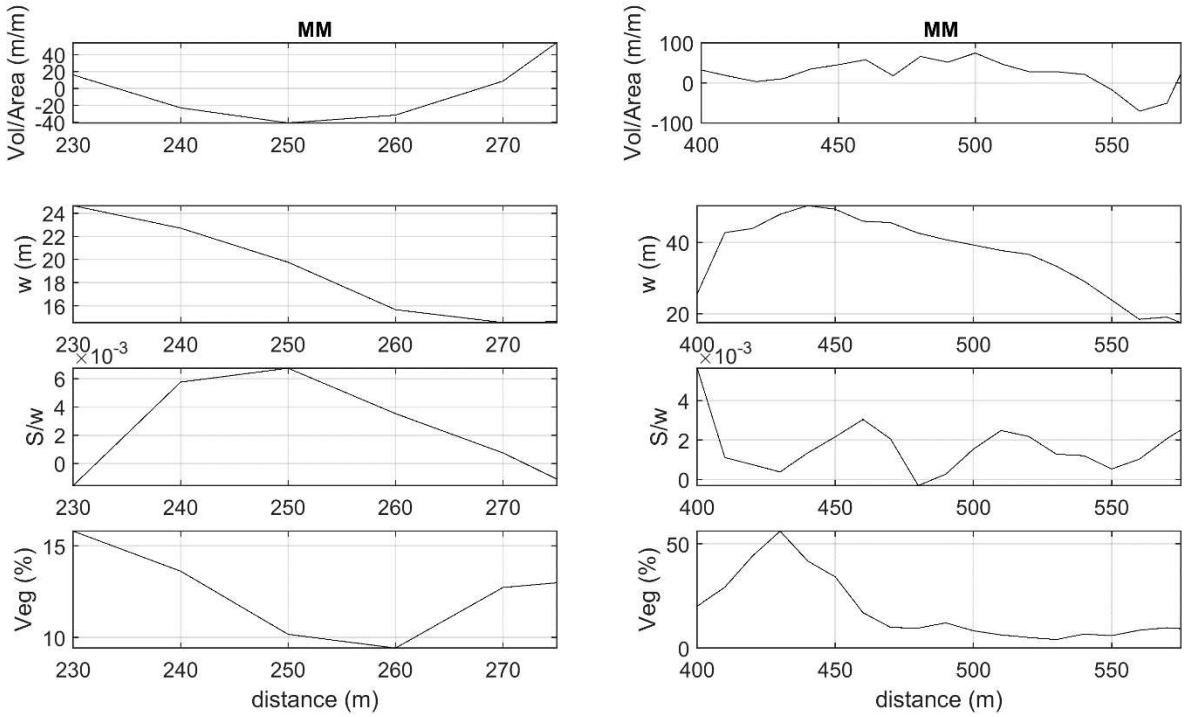

Figures 16 (Left) and 17 (Right): Longitudinal profiles of near-channel characteristics in areas of interest in MM

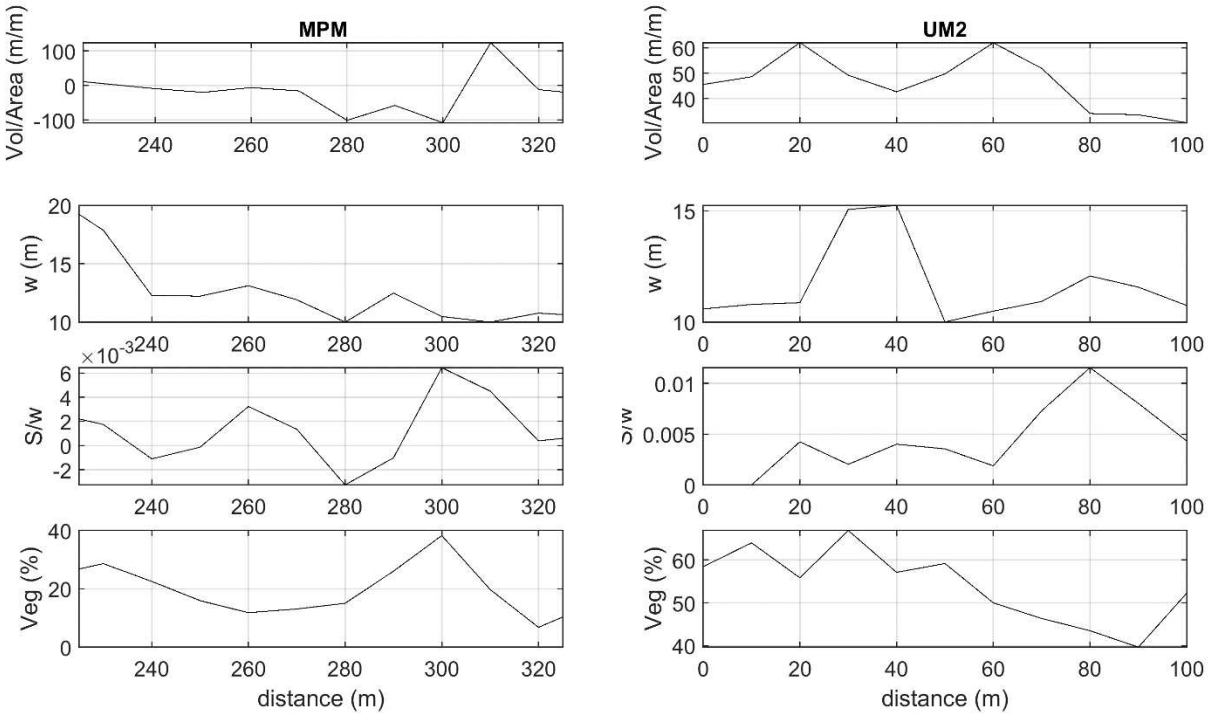

Figures 18 (Left) and 19 (Right): Longitudinal profiles of near-channel characteristics in areas of interest in MPM and UM2, respectively

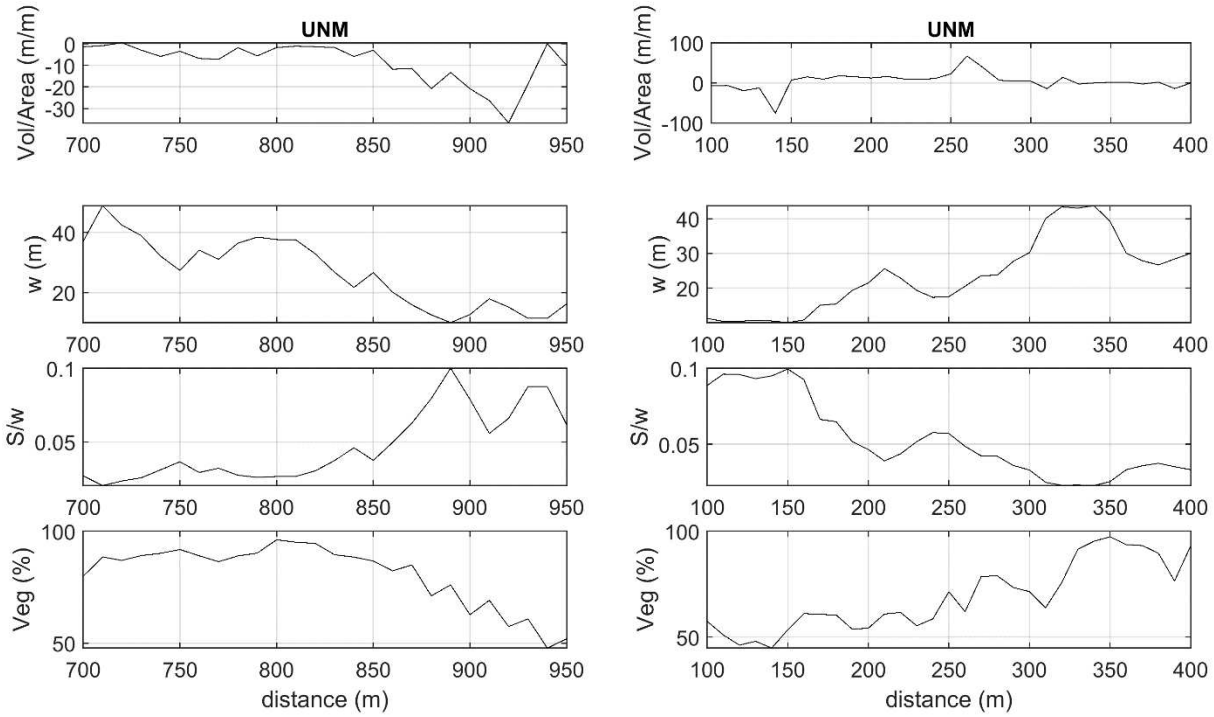

Figures 20 (Left) and 21 (Right): Longitudinal profiles of near-channel characteristics in areas of interest in UNM

(5) DISCUSSION

5.1 Large-Scale Volumetric Change

HWY 125 and Willow Creek reservoir are both directly affected by sediment volumes leaving the study watersheds and were both impacted significantly in the months and years after the East Troublesome Fire. Accurately quantifying sediment transport volumes is critical to the planning and application of post-fire mitigation strategies and the protection of downstream infrastructure. Hillslope erosion and deposition were the dominant contributors to sediment flux within the six study sites (Table 6). Similar LiDAR-based studies concluded that hillslope erosion was the dominant transport mechanism at the watershed scale (Rengers et al., 2021; Pelletier and Orem, 2014), and acknowledged watershed size to be an important factor in net sediment flux. In all but two of our study watersheds hillslope volumes were an order of magnitude larger than volumes stored or transported in the channel. Channel erosion in LPM contributed 44% of the total erosion, and channel deposition in MM was 30% of the total deposition. Additionally, all channels contributed more sediment per area than their hillslope counterparts, emphasizing the high capacity for transport and storage near and within channels (Table 7). Channel change was highly variable across the study sites, with each pair having one net erosional channel and one net depositional channel (Figure 9). LPM in particular contributed a large volume of sediment to Willow Creek. Normalized channel erosion and deposition were greatest for the lower pair of watersheds, followed by the middle pair, and the upper pair had the smallest values. Channels in LPM and LM2 were confined and had abundant transportable sediment available, along with very little vegetation in the near-channel areas, which were likely all contributing factors to the elevated transport rates in these watersheds. Normalized hillslope contributions were comparable

across all three pairs, with the upper pair having slightly larger values than the others. Knowledge of the sediment flux characteristics in each watershed allows us to identify where and to what extent mitigation strategies should be applied.

5.2 Controls on Topographic Change within and Across Watersheds

Our main objective of this study was to identify what watershed characteristics were contributing most to post-fire erosion and deposition, to better inform management strategies. By identifying areas where certain drivers are strongly correlated with erosion and deposition, we can gain insight on how to most effectively deploy mitigation efforts. In several cases, hillslope length had a particularly strong nonlinear relationship across the individual model runs. Erosion was positively correlated with hillslope length for lengths smaller than 250 m, and deposition was positively correlated for lengths greater than 250 m (Appendix Figures 10, 11, 13, 15 and 17). This phenomenon is corroborated by several established sediment transport equations including the Universal Soil Loss Equation (USLE), which predicts erosion to increase with length up to 120 m. The Revised Universal Soil Loss Equation (RUSLE) predicts this critical length to be around 300 m (Wischmeier and Smith, 1978; Renard et al., 1991). The physically based model Disturbed WEPP predicts sediment yield to increase with length up to 200 m, followed by decreasing yields after 250 m (Miller et al., 2011). Similar mulching studies (Prats et al., 2016; Schmeer et al., 2018) determined sediment yield decreased with slope length, and emphasized the effect of increasing complexity of slope characteristics over a large scale on total sediment yield. Because deposition is likely to begin as hillslope lengths increase, mulching efforts should be focused on hillslopes with lengths shorter than 300 m.

Total precipitation and maximum 60-minute intensity showed negligible correlations with erosion and deposition for all but one of the individual model runs but were significant contributors for both combined model runs. The MRMS data used to estimate precipitation for the study sites were gridded into fairly coarse 1 km^2 grid cells, which resulted in very little variability over the individual sites (Table 3). However, across all six watersheds this variability increased, and thus the true impact of these drivers could be more accurately defined. Total precipitation was negatively correlated with deposition, while 60-minute intensity was positively correlated, and both precipitation indices were positively correlated with erosion, which corroborates several recent studies that identify precipitation accumulation and intensity as some of the most important drivers of geomorphic change (Wagenbrenner et al., 2006; Robichaud et al., 2013a; Schmeer et al., 2018).

These studies, along with Benavides-Solorio and MacDonald (2005), identify bare ground coverage to be one of, if not the, strongest contributors to geomorphic change in post-fire landscapes. Our results are in agreement, with non-vegetated area contributing significantly in both the individual and combined models. In this study we combined bare soil, rock outcroppings, ground litter, and open water into a single classification for analysis (*BG*); in future studies the relationship between these more specialized ground covers, bare soil, and vegetation cover could be fleshed out by adding them as their own variables in the regression model. This distinction, along with variable success filtering vegetation, could be the cause of the varying correlations between *BG* and topographic change. Unfiltered vegetation resulted in positive and negative changes across all the basins; logically this would result in vegetation being positively correlated with erosion and deposition. Since our bare ground parameter was

calculated as all areas without vegetation, it makes sense that this could have influenced the bare ground correlation to be negative with erosion. Despite this variability, it is clear that *BG* plays an important role in post-fire sediment transport and should be included in the planning of mulching operations.

Average slope, *dNBR*, and width all displayed varying correlations and contribution levels across the model runs. Notably, slope was one of the strongest contributors in the catchments with the highest slopes, LM2, LPM, MPM and MM and one of the lowest contributors in the catchments with the lowest slopes, UM2, and UNM. This demonstrates that erosion and deposition are driven by slope in high-slope areas, but likely driven by other characteristics, such as absence of vegetation and precipitation, in low-slope areas. This emphasizes that for a mitigation strategy to be successful, it must be dynamic, and adapt to variable site conditions. *dNBR* displayed a nonlinear relationship with erosion and deposition, that identified a positive correlation with deposition for low severity values, and a positive correlation with erosion for moderate to high severity burn values. Burn severity has been shown to be a key contributor to geomorphic change, especially in the first 2-5 years post-fire for several reasons, including increased soil-water repellency and vegetation loss (Benavides-Solorio and MacDonald, 2005). As soil-water repellency is lost and vegetation regrows, *dNBR* will likely become a less effective predictor of geomorphic change, highlighting the necessity of acting quickly to prepare and apply models such as these. Width contributed marginally across all model runs, and had varying correlations with erosion and deposition but some of the model runs indicated a positive correlation between width and erosion for narrow average widths (<50 m).

When compared with other similar studies (e.g., Schmeer et al., 2018, Benavides-Solorio and MacDonald, 2005, Garter et al., 2014, Pelletier and Orem, 2014, Rengers et al. 2021), our model performed well. The performance of our models for the testing datasets was more varied and displayed lower correlations but several model runs produced testing results on a comparable level to the training datasets. While the goal of this study was not to produce a predictive model for erosion and deposition, these results emphasize that with a larger sample size of input data and careful collection and framing of data, bootstrap regression models could be a powerful and versatile tool for post-fire management.

5.3 Near-Channel Sediment Dynamics

Our volume estimates indicate that channels in post-fire environments are significant sources of sediment transport and storage and therefore should not be ignored in post-fire watershed management. Channel erosion was dominated by bank failure and incision in LPM and LM2 due to high degrees of confinement and abundant transportable sediment, likely a result of elevated hillslope contributions since the fire. Deposition in these sites was linked to areas where confinement lessened, leading to lower slopes and lessened stream power. The relationship between bare ground and width was a driving factor in the middle watersheds. This is likely due to a higher availability of mobile sediment in these areas. The upper watersheds were influenced considerably by dense riparian vegetation and elevated levels of floodplain connectivity. All sites indicate elevated levels of erosion and deposition and will continue to do so until either sediment loading rates decrease to pre-fire levels or the channels adapt sufficiently to handle the elevated levels.

Our study was limited to aerial data collection beginning two years post-fire. Extensive geomorphic changes had already occurred prior to the start of this project, denying us the ability to compare present channel conditions with pre-fire conditions. Additionally, we were limited to remote data collection techniques, so the drivers we analyzed are topographical in nature, parameters such as flowrate and sediment loading were not collected for this study. While these data would provide a more comprehensive analysis of our study sites, we were able to identify strong relationships between our selected parameters and channel erosion and deposition.

It has been shown that post-fire sediment contributions are responsible for upwards of 75% of the available sediment in the Colorado Front Range (Morris and Moses, 1987), and that pre-fire equilibrium is very rarely achieved prior to the next disturbance (Moody and Martin 2001), so heavily impacted areas in these sites may never return to their pre-fire morphology. With knowledge of the drivers of near-channel transport and storage, managers are better equipped to handle highly dynamic systems such as these.

5.4 Importance of Mulch

The regression models suggest that mulch coverage was not the most impactful driver behind topographic change at the watershed scale. Our analysis used proposed coverage areas, did not account for coverage variability on the ground and could not verify what the ground coverage rates were. These limitations may help to explain the low level of mulch contribution in the models. While mulch has been shown to be an effective mitigation strategy on the plot to hillslope scale, this is not the first study to indicate that it may be less effective as scale increases. Robichaud et al. (2013b) and Hubbert et al. (2012) found mulch to be effective at reducing erosion on plot-sized slopes but decreased in effectiveness when scaled to catchment-scale sites.

Fernandez et al. (2011) compared a mulch coverage rate of 45% on a 500 m slope to an untreated slope and found the mulch was unsuccessful at limiting transport. Studies have indicated that mulch coverage of at least 60% is necessary to achieve measurable impacts on erosion volumes (Girona-Garcia, 2021, Robichaud et al., 2000, Foltz and Copeland, 2009). No official coverage estimates were conducted for this study, but on-ground observations suggest that coverage sufficient to significantly affect large-scale sedimentation was not achieved over portions of the watersheds. Aerial mulching makes consistent coverage a difficult thing to achieve, small clumps of densely covered areas were observed with very little coverage in between them. In addition, high-intensity rainfall events were responsible for transporting mulch downslope where it was either trapped by ground litter or entered the channel itself.

Estimated volumes of erosion and deposition vary across mulched and unmulched portions of the study sites, with unmulched areas experiencing generally more erosion per area, and less deposition per area, though these differences fall within our uncertainty in all cases. With that being said, the combined models indicated a weak positive correlation between percent mulched area and deposition, and a small negative correlation between erosion and mulching for mulched area values above 60 and 80%, respectively. While these correlations are weak, and the individual model runs display differing relationships between mulched area and change, this may indicate that mulch played some role in stabilizing the slopes where it was applied. Additionally, mulch was applied in the areas identified as being at the highest risk for significant erosion.

Given these results and on-site observations, it is apparent that mulching operations could be improved to maximize their potential for limiting erosion and encouraging deposition. We

suggest mulch application at coverage rates greater than 60% should be focused on high-risk areas where mulch is capable of limiting erosion. Our study identifies high-slope areas that were burned severely and had a high percentage non-vegetated area as locations where mulching could best be focused.

5.5 Data Accuracy and Confidence Assessment

Remote sensing techniques and SfM processing have allowed for data collection and processing at very fine resolutions over increasingly large spatial scales. While the resolution of the data may be improving, it is necessary to ensure that the quality of the data is maintained throughout the collection and processing phases. The relationships identified in studies like this are completely dependent on the accuracy and confidence of the calculated volumes. Survey errors were combined with uncertainties from SfM processing to estimate vertical random error (VRE). Random horizontal error was much smaller than vertical error, so it was neglected from uncertainty calculations. Our September flight of UM2 was removed from analysis because it displayed systematic error that could not be reconciled. VRE was then propagated for the DoD calculation, and a 95% confidence level was applied. This gave us a discrete detection threshold at every point in the DoDs. Thresholding has been shown to be critical in accurately quantifying erosion and deposition volumes separately but can lead to underestimation of net changes and increases in uncertainty (Anderson, 2019). We used the propagated VRE grid to threshold out changes from our DoDs, but it is important to note that this likely filtered out widespread, small, changes that may have affected our final volume estimates.

Fixed-wing drones equipped with PPK present the next advancement in remote sensed geomorphic analysis. Our resolution, and maximum and mean propagated VRE, 4, 10 and 3.5

cm respectively, were similar, if not better, than similar studies (Ellett et al., 2019, East et al., 2021), and much improved compared to LiDAR-based detection (de Haas et al., 2021; Dai et al., 2022; Pelletier and Orem, 2014). Sediment movement due to rainsplash, sheetwash, and shallow rilling (<4 cm) are still unable to be quantified using these techniques, and due to uncertainty will likely remain out of reach. This study represents the cutting edge of remote sensed topographic change estimates and was successful in producing reasonable estimates of change volumes and their associated uncertainties.

Vegetation growth and decay, and felled trees were significant contributors to estimated volumes, so it was necessary to filter out their effects. SCP allowed us to classify each site based on RGB bands in the orthomosaic images and then filter our DoDs based on these classifications. SCP had varying levels of success over the six study sites. Areas of low vegetation and low shadowing, specifically LPM and LM2, were classified very effectively. SCP struggled the most in areas with low light and significant shadowing, dense vegetation, tops of trees, and vegetation that was a similar color to bare ground. This led to inconsistent and inadequate filtering at the edges of downed trees and the channel (All), in densely vegetated riparian zones (UNM, UM2 and MPM), and areas with dense tree coverage (MM, MPM, UM2). To mitigate these effects deposition was not quantified for the middle pair and all changes more than 2 m, the maximum in-channel change, were filtered out of UM2. Vegetation filtering presents another potential source of uncertainty, as riparian vegetation and dense hillslope groundcovers often capture and store large volumes of sediment. Any deposition occurring under vegetation that was filtered out was not quantified in the analysis, leading to potentially underestimated deposition volumes. Classification could have been improved by increasing the number of classification categories

from veg/nonveg, to include bare rock, shadowing, treetops, and any other site conditions present that do not directly fall into ground or vegetation. Additionally, more training polygons could be selected to provide a wider range of input signatures for the model to classify. Despite some of the shortcomings, SCP appears to be an effective classification tool that can be improved with more varied and extensive user input.

Despite the sources of uncertainty mentioned above we are confident in our calculations and model results for several reasons: (1) uncertainties were filtered out based on a 95% confidence interval, which is a conservative technique proven to mitigate impacts of anomalous values, giving us confidence that observed differences are actually occurring; (2) erosion and deposition changes due to vegetation were filtered out very effectively in UNM, LPM, and LM2 (>80% accuracy), and erosion change due to vegetation was filtered out adequately in MM, MPM, and UM2; (3) volumetric uncertainties were calculated based on an established uncertainty equation and reported alongside the calculated volumes; (4) a variety of site-specific and combined drivers of the geomorphic changes were assessed using our regression model, and its results were generally in agreement with previous similar studies; and (5) large uncertainties in UM2 and deposition in MM and MPM were not included in our analysis to mitigate effects of apparent change due to vegetation. For future studies, the timing of data collection is imperative to getting accurate and representative results of the processes occurring. First, data collection should begin as soon after the fire is extinguished as is feasible. The first two years post-fire are when the majority of geomorphic change occurs, and when mitigation techniques have the potential to be most impactful, so in order to better inform these management strategies data collection would ideally begin within a year. Secondly, aerial surveys should be conducted in the spring and fall

when vegetation is at its lowest to mitigate its effects. Lastly, as an extra precaution a flight should be conducted when vegetation is at its peak to maximize filtering efforts. This study presents results on a relatively unprecedented spatial scale and resolution, that can be a valuable asset for the prediction and management of post-fire sediment flux in mountainous regions. As mentioned, aerial mulching operations are time and cost intensive, so it is imperative to focus these projects on areas where mulch can have a measurable effect, likely on high-risk individual plots and hillslopes, rather than across entire watersheds.

(6) CONCLUSION

We conducted repeat aerial surveys of six, roughly 1 km^2, watershed outlets two years after the East Troublesome Wildfire, located in the Rocky Mountains of north central Colorado. Our first objective was to evaluate the spatial patterns of erosion and deposition within each site and across the entire study area. Erosion and deposition volumes were comparable across the six sites. Hillslope volumes were an order of magnitude larger than channel volumes for 4 of the sites and 2-3 times as large for the other two sites. Rills and gullies formed in the lower pair but were not detected in the other sites. Channels eroded more sediment per area than hillslopes, and displayed alternating patterns of erosion and deposition that were linked to several site-specific drivers. LPM channel was strongly net erosional and likely contributed a significant volume to downstream Willow Creek. Both erosion and deposition volumes were comparable in mulched and unmulched portions of the watersheds, and no significant difference could be identified. Our second objective was to assess the role of the channel as a transport and storage mechanism for excess sediment supplied by the hillslopes, and to identify topographic drivers of near channel behavior. All channels were dynamic with alternating areas of incision and aggradation. Width, stream power, and bare ground were strong predictors of near-channel changes. Our next objective was to determine the controls of sediment transport on a large scale, to better inform post-fire management and mitigation strategies. Our regression model highlighted the complex and dynamic relationships between our input drivers and change. Non-vegetated area, slope, length and precipitation metrics contributed strongly to multiple model runs, while mulch was indicated as a weak predictor for all model set-ups. Our final objective was to assess the impact of a watershed scale mulching operation. The results from this study agree with several others

that indicate mulch's impact decreases as scale increases. This does not mean that the technique should be abandoned or that there is nothing else to do in order to mitigate sediment flux. Mulch may be a more impactful, and cost-effective, treatment if applications are conducted on individual high-risk hillslopes immediately after the fire. Sediment transport out of these watersheds is a big concern as it poses a threat to downstream infrastructure and water quality. Our results indicate that channels are effective transporters of the excess sediment, so it may be advantageous to pair a hillslope mitigation strategy, such as mulching, with near-channel sinks or energy dissipation structures to reduce the sediment load leaving these watersheds. Lastly, this study shows that SfM photogrammetry using a fully PPK system can provide high-resolution, high-accuracy topographic datasets for large-scale projects in difficult terrain. The next steps for this project and similar projects in the future should include (1) surveying larger areas to continue to expand our knowledge of sediment dynamics at the watershed scale, (2) developing a consistent and reproducible approach to vegetation classification, and (3) introducing more parameters into regression models to better understand the complex relationship of erosion and deposition across scales.

REFERENCES

Addor, Nearing, G., Prieto, C., Newman, A. J., Le Vine, N., & Clark, M. P. (2018). A Ranking of Hydrological Signatures Based on Their Predictability in Space. Water Resources Research, 54(11), 8792–8812. https://doi.org/10.1029/2018WR022606

Anderson, Scott W. (2019). Uncertainty in quantitative analyses of topographic change: error mopropagation and the role of thresholding. Earth Surface Processes and Landforms, 44(5), 1015-1033. https://doi.org/10.1002/esp.4551

BAER (Burn Area Emergency Response). (2020). Soil Burn Severity Dataset for the EAST TROUBLESOME Fire occurring on the Arapaho & Roosevelt National Forests/Pawnee National Grassland National Forest. USDA Forest Service

Benavides-Solorio, J.D., MacDonald, L.H. (2001). Post-fire runoff and erosion from simulated rainfall on small plots, Colorado Front Range. Hydrological Processes 15, 2931–2952.

Benavides-Solorio, J.D., MacDonald, L.H. (2005). Measurement and prediction of post-fire erosion at the hillslope scale, Colorado Front Range. International Journal of Wildland Fire 14, 457–474.

Breiman, L. (2001). Random Forests. Machine learning, 45, 5-32.

Brogan, D. J., MacDonald, L. H., Nelson, P. A., & Morgan, J. A. (2019). Geomorphic complexity and sensitivity in channels to fire and floods in mountain catchments. Geomorphology, 337, 53-68.

Congedo, Luca, (2021). Semi-Automatic Classification Plugin: A Python tool for the download and processing of remote sensing images in QGIS. Journal of Open Source Software, 6(64), 3172.

Chapman, S.S., Griffith, G.E., Omernik, J.M., Price, A.B., Freeouf, J., and Schrupp, D.L. (2006). Ecoregions of Colorado (Map). Reston, Virginia, USGS.

Cook, K. L. and Dietze, M. (2019) Short Communication: A simple workflow for robust low-cost UAV-derived change detection without ground control points. Earth surface dynamics. [Online] 7 (4), 1009–1017.

Dai, Qian, W., Liu, A., Wang, C., Yang, X., Hu, G., & Tang, G. (2022). Monitoring and modeling sediment transport in space in small loess catchments using UAV-SfM photogrammetry. Catena (Giessen), 214, 106244–. https://doi.org/10.1016/j.catena.2022.106244

de Haas, T., Nijland, W., McArdell, B. W., & Kalthof, M. W. (2021). Case report: Optimization of topographic change detection with UAV structure-from-motion photogrammetry through survey co-alignment. Frontiers in Remote Sensing, 2, 5.

East, Amy E., et al. “Watershed Sediment Yield Following the 2018 Carr Fire, Whiskeytown National Recreation Area, Northern California.” Earth and Space Science (Hoboken, N.J.), vol. 8, no. 9, John Wiley & Sons, Inc, 2021, https://doi.org/10.1029/2021EA001828.

Ellett, Nicholas G., et al. “Partitioned by Process: Measuring Post-fire Debris-flow and Rill Erosion with Structure from Motion Photogrammetry.” Earth Surface Processes and Landforms, vol. 44, no. 15, Wiley Subscription Services, Inc, 2019, pp. 3128–46, https://doi.org/10.1002/esp.4728.

Eng, Grantham, T. E., Carlisle, D. M., & Wolock, D. M. (2017). Predictability and selection of hydrologic metrics in riverine ecohydrology. Freshwater Science, 36(4), 915–926. https://doi.org/10.1086/694912

Foltz, & Copeland, N. S. (2009). Evaluating the efficacy of wood shreds for mitigating erosion. Journal of Environmental Management, 90(2), 779–785. https://doi.org/10.1016/j.jenvman.2008.01.006

Foltz, R.B., Wagenbrenner, N.S. (2010). An evaluation of three wood shred blends for post-fire erosion control using indoor simulated rain events on small plots. Catena 80, 86–94.

Fonstad, M.A., Dietrich, J.T., Courville, B.C., Jensen, J.L. and Carbonneau, P.E. (2013), Topographic structure from motion: a new development in photogrammetric measurement. Earth Surf. Process. Landforms, 38: 421-430. https://doi.org/10.1002/esp.3366

Girona-García, A, et al. “Effectiveness of Post-Fire Soil Erosion Mitigation Treatments: A Systematic Review and Meta-Analysis.” Earth-Science Reviews, vol. 217, 2021, p. 103611., https://doi.org/10.1016/j.earscirev.2021.103611.

Hubbert, K.R., Wohlgemuth, P.M., Beyers, J.L., 2012. Effects of hydromulch on post-fire erosion and plant recovery in chaparral shrublands of southern California. International Journal of Wildland Fire 21, 155–167.

James, Robson, S., & Smith, M.W. (2017). 3-D uncertainty-based topographic change detection with structure-from-motion photogrammetry: precision maps for ground control and directly georeferenced surveys: 3-D uncertainty-based change detection for SfM surveys. Earth Surface Processes and Landforms, 42(12), 1769-1788. https://doi.org/10.1002/esp.4125

James, M. R., Antoniazza, G., Robson, S., and Lane, S. N. (2020). Mitigating systematic error in topographic models for geomorphic change detection: accuracy, precision and considerations beyond off-nadir imagery. Earth Surf. Process. Landforms, 45: 2251– 2271.

Kampf, Gannon, B. M., Wilson, C., Saavedra, F., Miller, M. E., Heldmyer, A., Livneh, B., Nelson, P., & MacDonald, L. (2020). PEMIP: Post-fire erosion model inter-comparison project. Journal of Environmental Management, 268, 110704–110704. https://doi.org/10.1016/j.jenvman.2020.110704

Miller, J.D., Safford, H.D., Crimmins, M. et al. Quantitative Evidence for Increasing Forest Fire Severity in the Sierra Nevada and Southern Cascade Mountains, California and Nevada, USA. Ecosystems 12, 16–32 (2009). https://doi.org/10.1007/s10021-008-9201-9

Miller, M.E., MacDonald, L.H., Robichaud, P.R., Elliot, W.J., 2011. Predicting post-fire hillslope erosion in forest lands of the western United States. Int. J. Wildland Fire 20 (8), 982–999.

Miller, Carlisle, D. M., Wolock, D. M., & Wieczorek, M. (2018). A Database of Natural Monthly Streamflow Estimates from 1950 to 2015 for the Conterminous United States. Journal of the American Water Resources Association, 54(6), 1258–1269. https://doi.org/10.1111/1752-1688.12685

Moody, John A., and Deborah A. Martin. "Initial Hydrologic and Geomorphic Response Following a Wildfire in the Colorado Front Range." Earth Surface Processes and Landforms, vol. 26, no. 10, 14 Feb. 2001, pp. 1049–1070., https://doi.org/10.1002/esp.253.

Morris, Scott E., and Todd A. Moses. "Forest Fire and the Natural Soil Erosion Regime in the Colorado Front Range." Annals of the Association of American Geographers, vol. 77, no. 2, June 1987, pp. 245–254., https://doi.org/10.1111/j.1467-8306.1987.tb00156.x.

Over, Jin-Si R. Processing Coastal Imagery with Agisoft Metashape Professional Edition, Version 1.6—Structure from Motion Workflow Documentation. Reston, Virginia: U.S. Department of the Interior, U.S. Geological Survey, 2021. Print.

Pelletier, J. D., & Orem, C. A. (2014). How do sediment yields from post-wildfire debris-laden flows depend on terrain slope, soil burn severity class, and drainage basin area? Insights from airborne-LiDAR change detection. Earth Surface Processes and Landforms, 39(13), 1822–1832.

Prats, Sergio Alegre, et al. "Mid-Term and Scaling Effects of Forest Residue Mulching on Post-Fire Runoff and Soil Erosion." Science of The Total Environment, vol. 573, 2016, pp. 1242–1254., https://doi.org/10.1016/j.scitotenv.2016.04.064.

PRISM Climate Group, Oregon State University, http://prism.oregonstate.edu

Renard, K. G., Foster, G. R., Weesies, G. A., & Porter, J. P. (1991). RUSLE: Revised universal soil loss equation. Journal of soil and Water Conservation, 46(1), 30-33.

Rengers, F. K., McGuire, L. A., Kean, J. W., Staley, D. M., Dobre, M., Robichaud, P. R., & Swetnam, T. (2021). Movement of sediment through a burned landscape: Sediment volume observations and model comparisons in the San Gabriel Mountains, California, USA. Journal of Geophysical Research: Earth Surface, 126, e2020JF006053.

Robichaud, P.R., Beyers, J.L., Neary, D.G. (2000). Evaluating the Effectiveness of Postfire Rehabilitation Treatments. General Technical Report, RMRS-GTR-63. U.S. Department of Agriculture, Forest Service, Rocky Mountain Research Station, Fort Collins, CO.

Robichaud P.R. (2005). Measurement of post-fire hillslope erosion to evaluate and model rehabilitation treatment effectiveness and recovery. International Journal of Wildland Fire 14, 475-485.

Robichaud, P.R., Ashmun, L.E., Sims, B.D. (2010a). Post-Fire Treatment Effectiveness for Hillslope Stabilization. General Technical Report, RMRS-GTR-240. U.S. Department of Agriculture, Forest Service, Rocky Mountain Research Station, Fort Collins, CO.

Robichaud, P. R., Lewis, S. A., Wagenbrenner, J. W., Ashmun, L. E., & Brown, R. E. (2013). Post-fire mulching for runoff and erosion mitigation: Part I: Effectiveness at reducing hillslope erosion rates. CATENA, 105, 75–92.

Robichaud, P. R., Wagenbrenner, J. W., Lewis, S. A., Ashmun, L. E., Brown, R. E., & Wohlgemuth, P. M. (2013). Post-fire mulching for runoff and erosion mitigation Part II: Effectiveness in reducing runoff and sediment yields from small catchments. Catena, 105, 93-111.

Rolstad, C., Haug, T., Denby, B. (2009). Spatially integrated geodetic glacier mass balance and its uncertainty based on geostatistical analysis: application to the western Svartisen ice cap, Norway. J. Glaciol. 55 (192), 666–680.

Schmeer, Sarah R., et al. “Empirical Models of Annual Post-Fire Erosion on Mulched and Unmulched Hillslopes.” CATENA, vol. 163, 2018, pp. 276–287., https://doi.org/10.1016/j.catena.2017.12.029.

Schmeer, S. R., Kampf, S. K., MacDonald, L. H., Hewitt, J., & Wilson, C. (2018). Empirical models of annual post-fire erosion on mulched and unmulched hillslopes. Catena, 163, 276-287.

Soil Survey Staff, Natural Resources Conservation Service, United States Department of Agriculture. Web Soil Survey. Available online https://websoilsurvey.sc.egov.usda.gov/App/WebSoilSurvey.aspx . Accessed 05/27/2023.

Swanson, F. J. 1981. Fire and geomorphic processes. In Fire regime and ecosystem properties, ed. H.A. Mooney, T.M. Bonnicksen, N.L. Christensen, J.E. Lotan, and W.A. Reiners, pp. 401-20. USDA Forest Service General Technical Report WO-26. Washington, D.C.: U.S. Government Printing Office.

Wagenbrenner, J.W., MacDonald, L.H., Rough, D. (2006). Effectiveness of three post-fire rehabilitation treatments in the Colorado Front Range. Hydrological Processes 20, 2989–3006.

Westerling AL, Hidalgo HG, Cayan DR, Swetnam TW. Warming and earlier spring increase western U.S. forest wildfire activity. Science. 2006 Aug 18;313(5789):940-3. doi: 10.1126/science.1128834. Epub 2006 Jul 6. PMID: 16825536.

Wischmeier, W.H., Smith, D.D. (1978). Predicting Rainfall Erosion Losses – A Guide to Conservation Planning. U.S. Department of Agriculture (Handbook No. 537).

Wilson, C., Kampf, S. K., Wagenbrenner, J. W., & MacDonald, L. H. (2018). Rainfall thresholds for post-fire runoff and sediment delivery from plot to watershed scales. Forest ecology and management, 430, 346-356.

Zhang, J., Howard, K., Langston, C., Kaney, B., Qi, Y., Tang, L., Grams, H., Wang, Y., Cockcks, S., Martinaitis, S., Arthur, A., Cooper, K., Brogden, J., & Kitzmillller, D. (2016). Multi-Radar Multi-Sensor (MRMS) quantitative precipitation estimation: Initial operating capabilities. Bulletin of the American Meteorological Society, 97(4), 621–638. https://doi.org/10.1175/BAMS-D-14-00174.1

Zipper, S. C., Hammond, J. C., Shanafield, M., Zimmer, M., Datry, T., Jones, C. N., … & Allen, D. C. (2021). Pervasive changes in stream intermittency across the United States. Environmental Research Letters, 16(8), 084033.

APPENDIX

LPM Erosion	log(Ero/Area)	w	L	MI60	P	S	dNBR	BG	M
log(Ero/Area)	1.000	0.095	0.122	-0.011	-0.422	0.441	-0.510	-0.161	-0.315
w	0.095	1.000	0.446	-0.401	0.096	-0.152	0.165	0.149	-0.058
L	0.122	0.446	1.000	-0.129	-0.228	0.001	0.126	-0.085	0.133
MI60	-0.011	-0.401	-0.129	1.000	0.260	0.060	0.196	-0.150	0.442
P	-0.422	0.096	-0.228	0.260	1.000	-0.304	0.443	0.123	0.359
S	0.441	-0.152	0.001	0.060	-0.304	1.000	-0.729	-0.108	-0.414
dNBR	-0.510	0.165	0.126	0.196	0.443	-0.729	1.000	-0.091	0.832
BG	-0.161	0.149	-0.085	-0.150	0.123	-0.108	-0.091	1.000	-0.140
M	-0.315	-0.058	0.133	0.442	0.359	-0.414	0.832	-0.140	1.000

Appendix Figure 1: Pearson correlation coefficients for LPM erosion model

LPM Deposition	log(Dep/Area)	w	L	MI60	P	S	dNBR	BG	M
log(Dep/Area)	1.000	0.210	-0.050	0.067	0.072	0.074	0.212	-0.071	0.340
w	0.210	1.000	0.446	-0.401	0.096	-0.152	0.165	0.149	-0.058
L	-0.050	0.446	1.000	-0.129	-0.228	0.001	0.126	-0.085	0.133
MI60	0.067	-0.401	-0.129	1.000	0.260	0.060	0.196	-0.150	0.442
P	0.072	0.096	-0.228	0.260	1.000	-0.304	0.443	0.123	0.359
S	0.074	-0.152	0.001	0.060	-0.304	1.000	-0.729	-0.108	-0.414
dNBR	0.212	0.165	0.126	0.196	0.443	-0.729	1.000	-0.091	0.832
BG	-0.071	0.149	-0.085	-0.150	0.123	-0.108	-0.091	1.000	-0.140
M	0.340	-0.058	0.133	0.442	0.359	-0.414	0.832	-0.140	1.000

Appendix Figure 2: Pearson correlation coefficients for LPM deposition model

LM2 Erosion	log(Ero/Area)	w	L	MI60	P	S	dNBR	BG	M
log(Ero/Area)	1.000	0.299	-0.465	-0.447	0.372	0.798	-0.034	-0.267	-0.358
w	0.299	1.000	0.017	-0.193	0.193	0.377	0.034	0.374	-0.311
L	-0.465	0.017	1.000	0.533	-0.405	-0.408	-0.034	0.447	0.315
MI60	-0.447	-0.193	0.533	1.000	-0.832	-0.329	-0.210	0.208	0.491
P	0.372	0.193	-0.405	-0.832	1.000	0.256	0.180	-0.074	-0.338
S	0.798	0.377	-0.408	-0.329	0.256	1.000	-0.733	-0.073	-0.404
dNBR	-0.034	0.034	-0.034	-0.210	0.180	-0.733	1.000	0.178	0.164
BG	-0.267	0.374	0.447	0.208	-0.074	-0.073	0.178	1.000	0.202
M	-0.358	-0.311	0.315	0.491	-0.338	-0.404	0.164	0.202	1.000

Appendix Figure 3: Pearson correlation coefficients for LM2 erosion model

LM2 Deposition	log(Dep/Area)	w	L	MI60	P	S	dNBR	BG	M
log(Dep/Area)	1.000	0.082	-0.448	-0.148	0.090	0.375	0.011	-0.185	-0.059
w	0.082	1.000	0.017	-0.193	0.193	0.377	0.034	0.374	-0.311
L	-0.448	0.017	1.000	0.533	-0.405	-0.408	-0.034	0.447	0.315
MI60	-0.148	-0.193	0.533	1.000	-0.832	-0.329	-0.210	0.208	0.491
P	0.090	0.193	-0.405	-0.832	1.000	0.256	0.180	-0.074	-0.338
S	0.375	0.377	-0.408	-0.329	0.256	1.000	-0.733	-0.073	-0.404
dNBR	0.011	0.034	-0.034	-0.210	0.180	-0.733	1.000	0.178	0.164
BG	-0.185	0.374	0.447	0.208	-0.074	-0.073	0.178	1.000	0.202
M	-0.059	-0.311	0.315	0.491	-0.338	-0.404	0.164	0.202	1.000

Appendix Figure 4: Pearson correlation coefficients for LM2 deposition model

MPM Erosion	log(Ero/Area)	w	L	MI60	P	S	dNBR	BG	M
log(Ero/Area)	1.000	-0.142	0.133	0.017	-0.128	0.026	-0.170	0.183	0.000
w	-0.142	1.000	-0.038	0.269	-0.001	-0.052	-0.254	-0.279	0.000
L	0.133	-0.038	1.000	-0.097	-0.045	0.023	0.330	0.311	0.000
MI60	0.017	0.269	-0.097	1.000	-0.549	0.147	-0.223	-0.079	0.000
P	-0.128	-0.001	-0.045	-0.549	1.000	-0.036	-0.033	-0.418	0.000
S	0.026	-0.052	0.023	0.147	-0.036	1.000	0.029	-0.051	0.000
dNBR	-0.170	-0.254	0.330	-0.223	-0.033	0.029	1.000	0.468	0.000
BG	0.183	-0.279	0.311	-0.079	-0.418	-0.051	0.468	1.000	0.000
M	0.000	0.000	0.000	0.000	0.000	0.000	0.000	0.000	1.000

Appendix Figure 5: Pearson correlation coefficients for MPM erosion model

MM Erosion	log(Ero/Area)	w	L	MI60	P	S	dNBR	BG	M
log(Ero/Area)	1.000	-0.050	-0.001	-0.032	-0.013	0.278	0.273	0.134	0.365
w	-0.050	1.000	0.046	-0.156	-0.101	-0.153	-0.263	-0.235	-0.268
L	-0.001	0.046	1.000	0.276	0.319	0.057	0.313	0.507	0.313
MI60	-0.032	-0.156	0.276	1.000	0.970	-0.056	0.064	0.329	0.083
P	-0.013	-0.101	0.319	0.970	1.000	-0.037	0.026	0.343	0.062
S	0.278	-0.153	0.057	-0.056	-0.037	1.000	0.161	0.190	0.156
dNBR	0.273	-0.263	0.313	0.064	0.026	0.161	1.000	0.741	0.844
BG	0.134	-0.235	0.507	0.329	0.343	0.190	0.741	1.000	0.695
M	0.365	-0.268	0.313	0.083	0.062	0.156	0.844	0.695	1.000

Appendix Figure 6: Pearson correlation coefficients for MM erosion model

UNM Erosion	log(Ero/Area)	w	L	MI60	P	S	dNBR	BG	M
log(Ero/Area)	1.000	0.307	-0.021	0.191	-0.375	-0.375	-0.024	-0.739	0.000
w	0.307	1.000	0.179	0.047	-0.220	-0.220	0.061	-0.330	0.000
L	-0.021	0.179	1.000	0.007	0.087	0.087	-0.082	0.076	0.000
S	0.191	0.047	0.007	1.000	-0.128	-0.128	-0.072	-0.161	0.000
MI60	-0.375	-0.220	0.087	-0.128	1.000	1.000	-0.033	0.286	0.000
P	-0.375	-0.220	0.087	-0.128	1.000	1.000	-0.033	0.286	0.000
dNBR	-0.024	0.061	-0.082	-0.072	-0.033	-0.033	1.000	-0.029	0.000
BG	-0.739	-0.330	0.076	-0.161	0.286	0.286	-0.029	1.000	0.000
M	0.000	0.000	0.000	0.000	0.000	0.000	0.000	0.000	1.000

Appendix Figure 7: Pearson correlation coefficients for UNM erosion model

UNM Deposition	log(Dep/Area)	w	L	MI60	P	S	dNBR	BG	M
log(Dep/Area)	1.000	0.045	0.309	-0.009	-0.087	-0.087	-0.107	-0.371	0.000
w	0.045	1.000	0.179	0.047	-0.220	-0.220	0.061	-0.330	0.000
L	0.309	0.179	1.000	0.007	0.087	0.087	-0.082	0.076	0.000
S	-0.009	0.047	0.007	1.000	-0.128	-0.128	-0.072	-0.161	0.000
MI60	-0.087	-0.220	0.087	-0.128	1.000	1.000	-0.033	0.286	0.000
P	-0.087	-0.220	0.087	-0.128	1.000	1.000	-0.033	0.286	0.000
dNBR	-0.107	0.061	-0.082	-0.072	-0.033	-0.033	1.000	-0.029	0.000
BG	-0.371	-0.330	0.076	-0.161	0.286	0.286	-0.029	1.000	0.000
M	0.000	0.000	0.000	0.000	0.000	0.000	0.000	0.000	1.000

Appendix Figure 8: Pearson correlation coefficients for UNM deposition model

UM2	log(Ero/Area)	log(Dep/Area)	w	L	MI60	P	S	dNBR	BG	M
log(Ero/Area)	1.000	0.778	-0.097	0.287	-0.221	-0.397	-0.486	-0.522	-0.777	-0.336
log(Dep/Area)	0.778	1.000	-0.120	0.183	-0.091	-0.598	-0.643	-0.750	-0.805	-0.519
w	-0.097	-0.120	1.000	0.110	0.012	0.063	0.078	0.138	0.030	-0.119
L	0.287	0.183	0.110	1.000	-0.483	0.025	-0.034	-0.154	-0.170	0.015
MI60	-0.221	-0.091	0.012	-0.483	1.000	0.131	0.269	0.334	0.209	0.036
P	-0.397	-0.598	0.063	0.025	0.131	1.000	0.431	0.728	0.704	0.803
S	-0.486	-0.643	0.078	-0.034	0.269	0.431	1.000	0.721	0.566	0.294
dNBR	-0.522	-0.750	0.138	-0.154	0.334	0.728	0.721	1.000	0.800	0.587
BG	-0.777	-0.805	0.030	-0.170	0.209	0.704	0.566	0.800	1.000	0.636
M	-0.336	-0.519	-0.119	0.015	0.036	0.803	0.294	0.587	0.636	1.000

Appendix Figure 9: Pearson correlation coefficients for UM2 erosion and deposition models

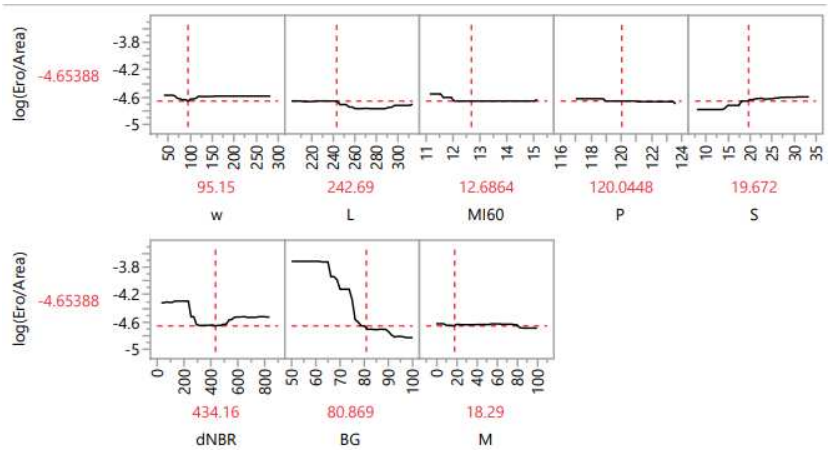

Appendix Figure 10: Partial dependence plots for UM2 erosion model

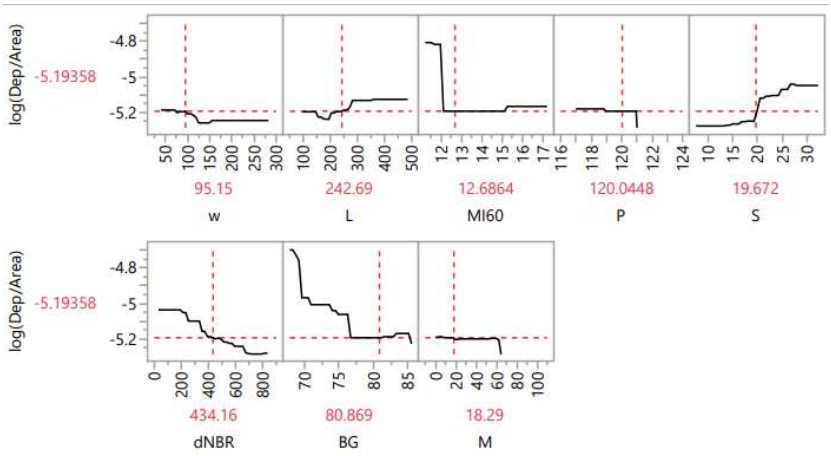

Appendix Figure 11: Partial dependence plots for UM2 deposition model

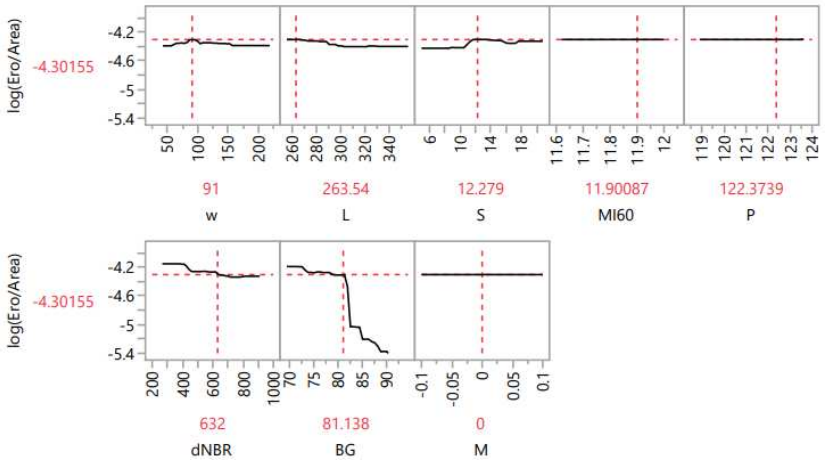

Appendix Figure 12: Partial dependence plots for UNM erosion model

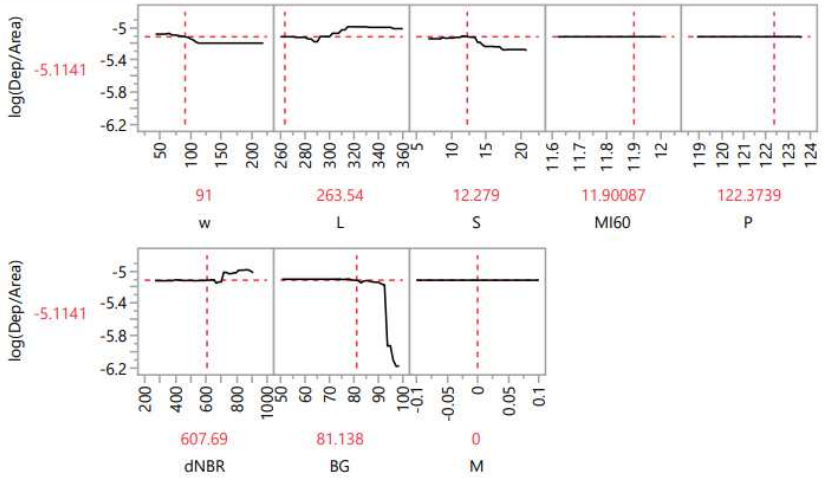

Appendix Figure 13: Partial dependence plots for UNM deposition model

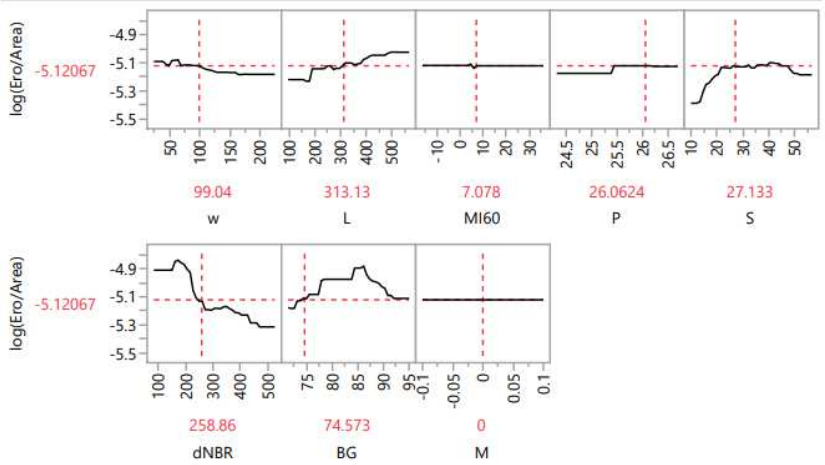

Appendix Figure 14: Partial dependence plots for MPM erosion model

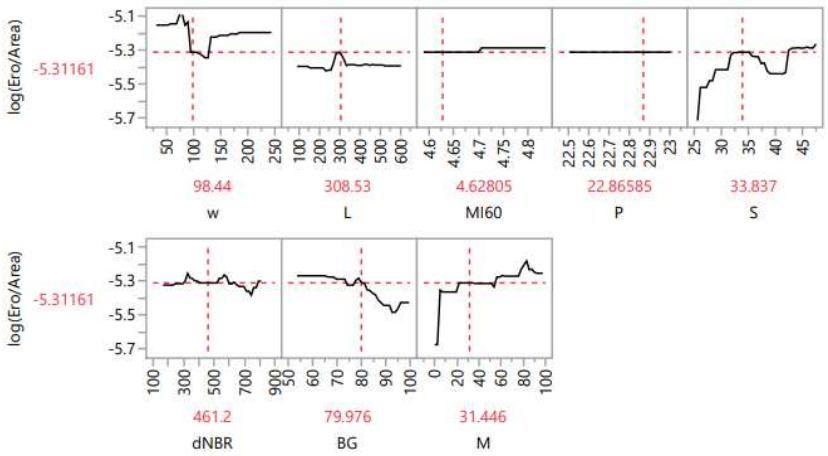

Appendix Figure 15: Partial dependence plots for MM erosion model

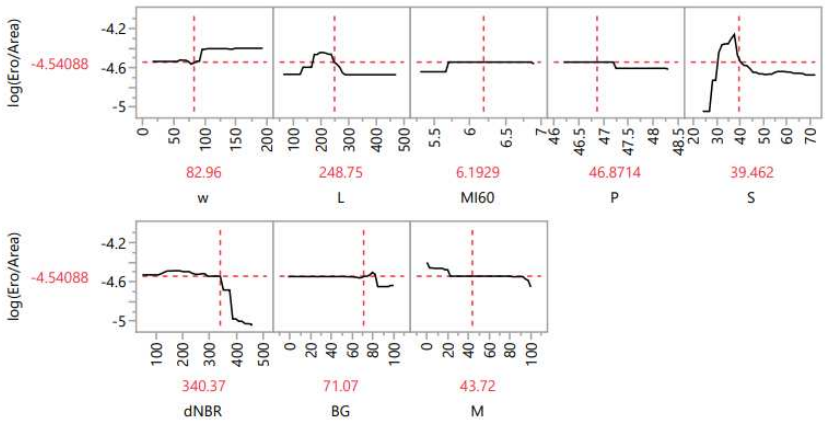

Appendix Figure 16: Partial dependence plots for LPM erosion model

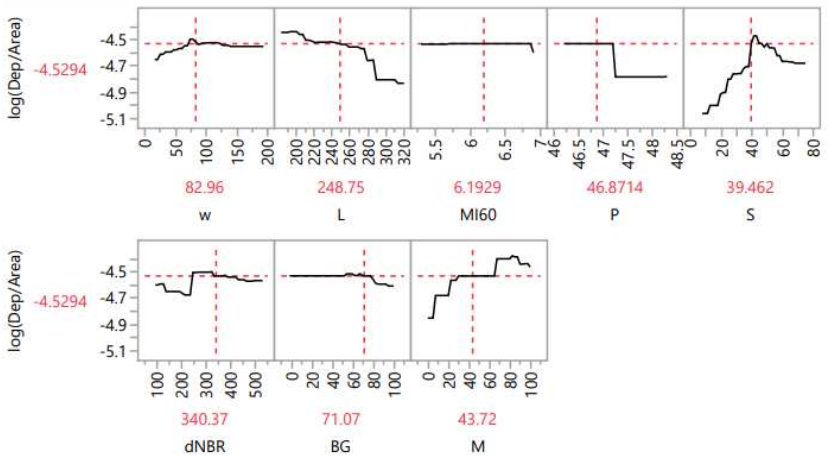

Appendix Figure 17: Partial dependence plots for LPM deposition model

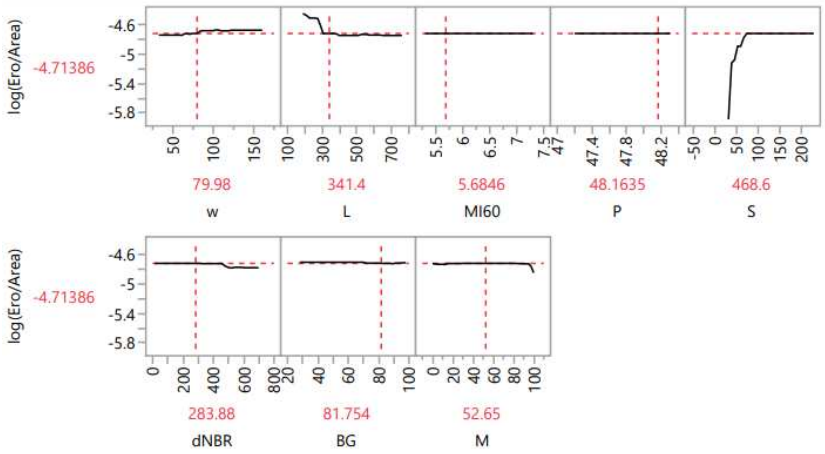

Appendix Figure 18: Partial dependence plots for LM2 erosion model

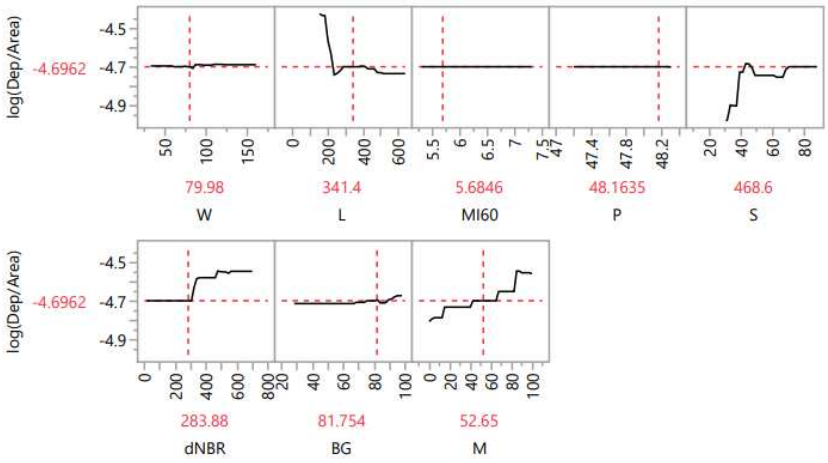

Appendix Figure 19: Partial dependence plots for LM2 deposition model

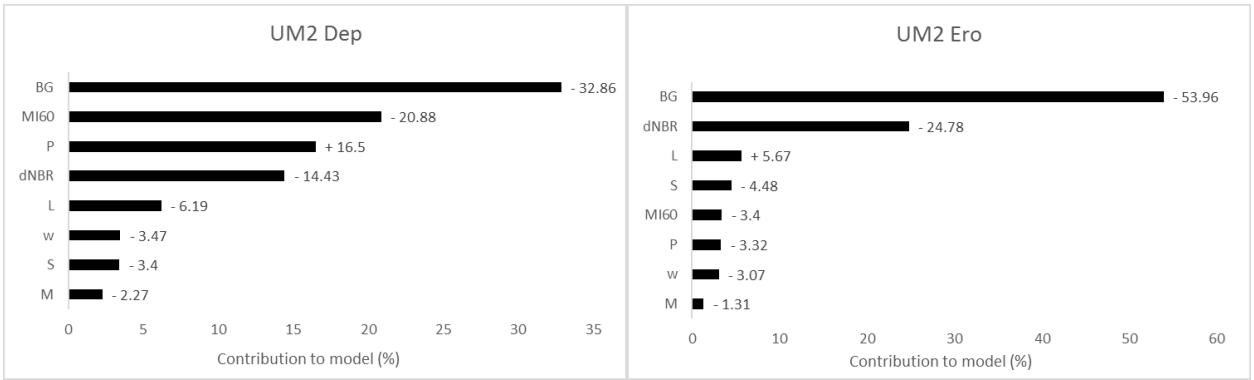

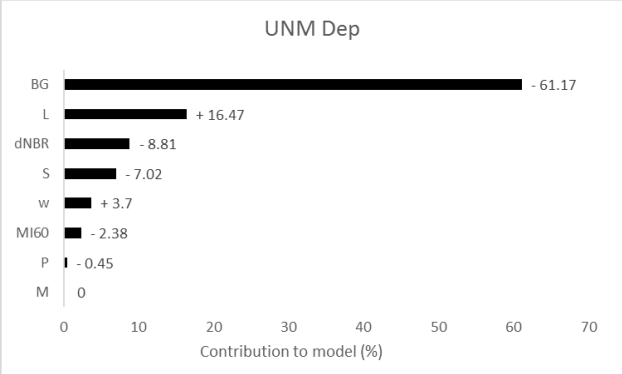
UNM Dep
BG - 61.17
L + 16.47
dNBR - 8.81
S - 7.02
w + 3.7
MI60 - 2.38
P - 0.45
M 0
0 10 20 30 40 50 60 70
Contribution to model (%)

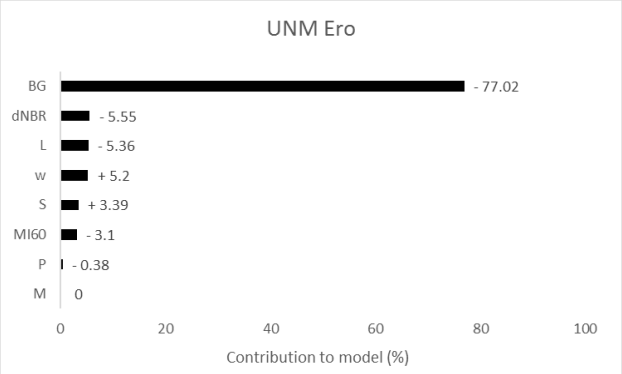
UNM Ero
BG - 77.02
dNBR - 5.55
L - 5.36
w + 5.2
S + 3.39
MI60 - 3.1
P - 0.38
M 0
0 20 40 60 80 100
Contribution to model (%)

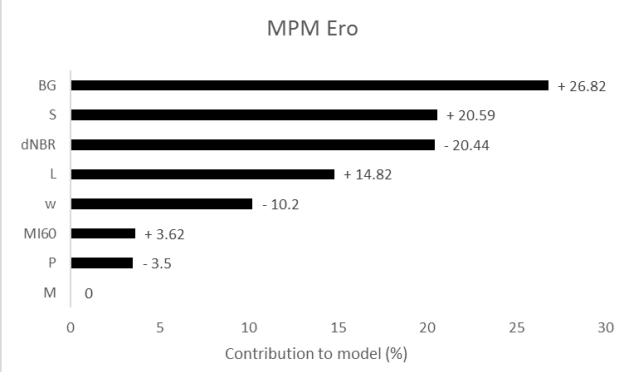
MPM Ero
BG + 26.82
S + 20.59
dNBR - 20.44
L + 14.82
w - 10.2
MI60 + 3.62
P - 3.5
M 0
0 5 10 15 20 25 30
Contribution to model (%)

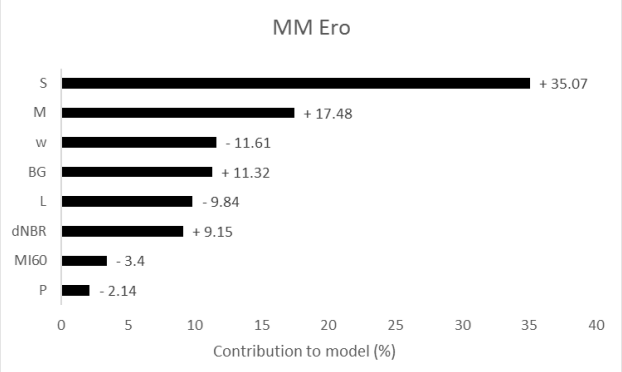
MM Ero
S + 35.07
M + 17.48
w - 11.61
BG + 11.32
L - 9.84
dNBR + 9.15
MI60 - 3.4
P - 2.14
0 5 10 15 20 25 30 35 40
Contribution to model (%)

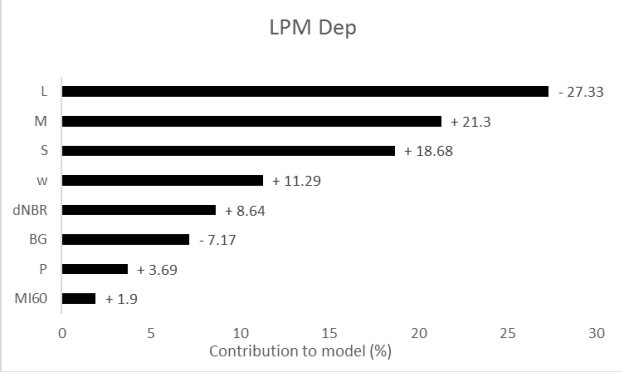
LPM Dep
L - 27.33
M + 21.3
S + 18.68
w + 11.29
dNBR + 8.64
BG - 7.17
P + 3.69
MI60 + 1.9
0 5 10 15 20 25 30
Contribution to model (%)

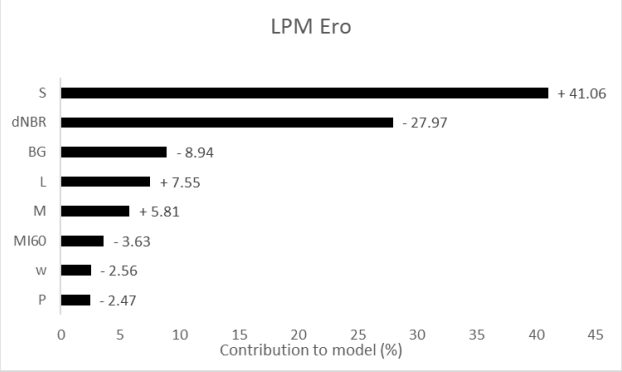
LPM Ero
S + 41.06
dNBR - 27.97
BG - 8.94
L + 7.55
M + 5.81
MI60 - 3.63
w - 2.56
P - 2.47
0 5 10 15 20 25 30 35 40 45
Contribution to model (%)

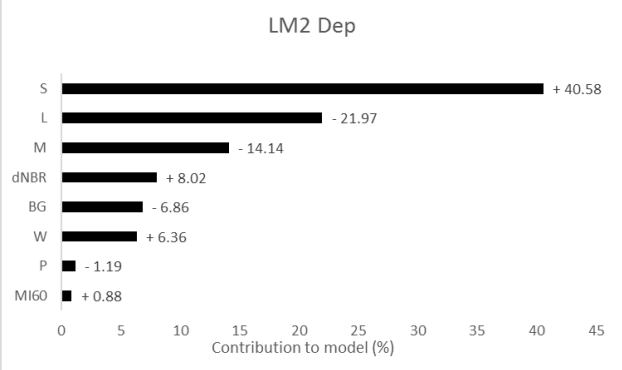
LM2 Dep
S + 40.58
L - 21.97
M - 14.14
dNBR + 8.02
BG - 6.86
W + 6.36
P - 1.19
MI60 + 0.88
0 5 10 15 20 25 30 35 40 45
Contribution to model (%)

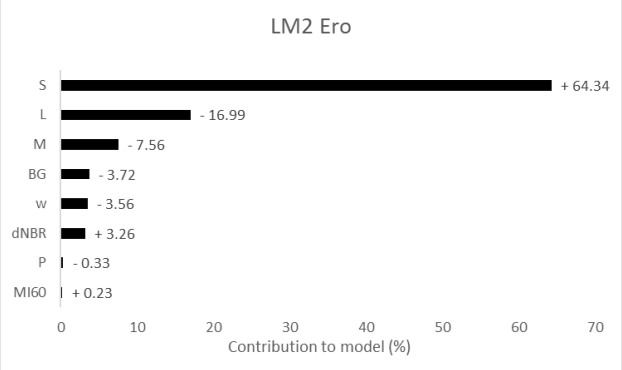
LM2 Ero
S + 64.34
L - 16.99
M - 7.56
BG - 3.72
w - 3.56
dNBR + 3.26
P - 0.33
MI60 + 0.23
0 10 20 30 40 50 60 70
Contribution to model (%)

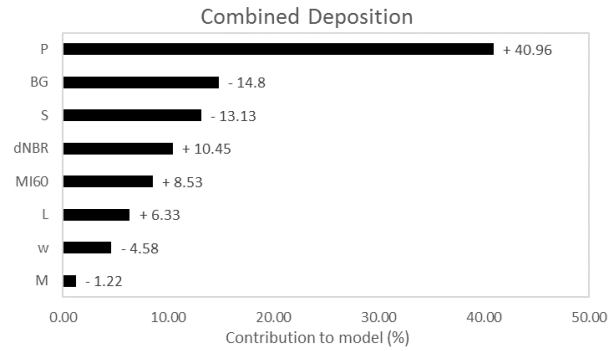

Appendix Figures 20-30: Model contributions for models not shown in text

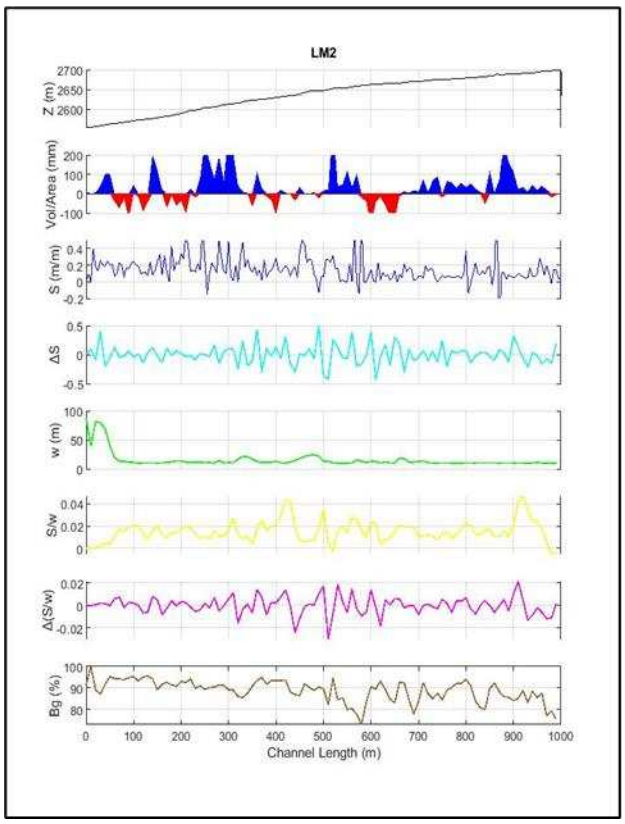

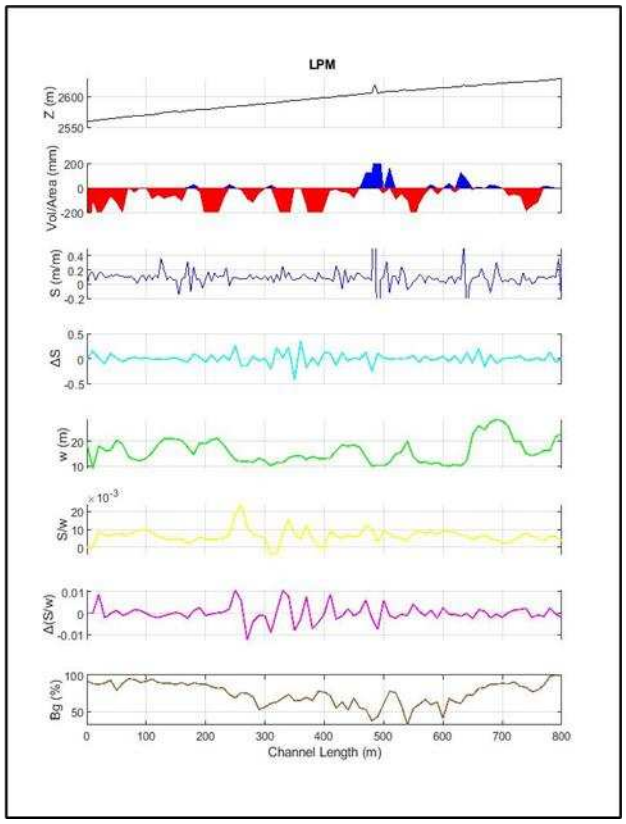

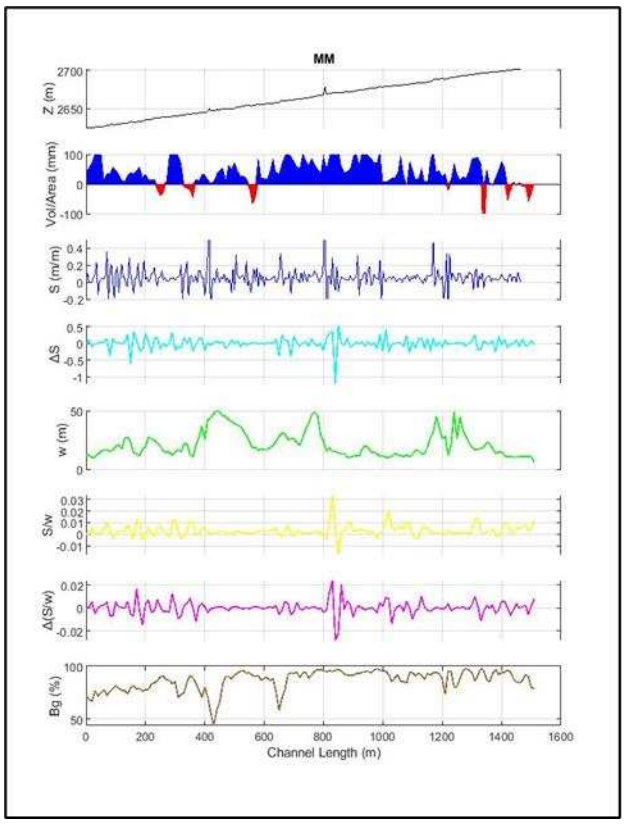
MM
Z (m)
Vol/Area (mm)
S (m/m)
ΔS
w (m)
S/w
Δ(S/w)
Bg (%)
Channel Length (m)

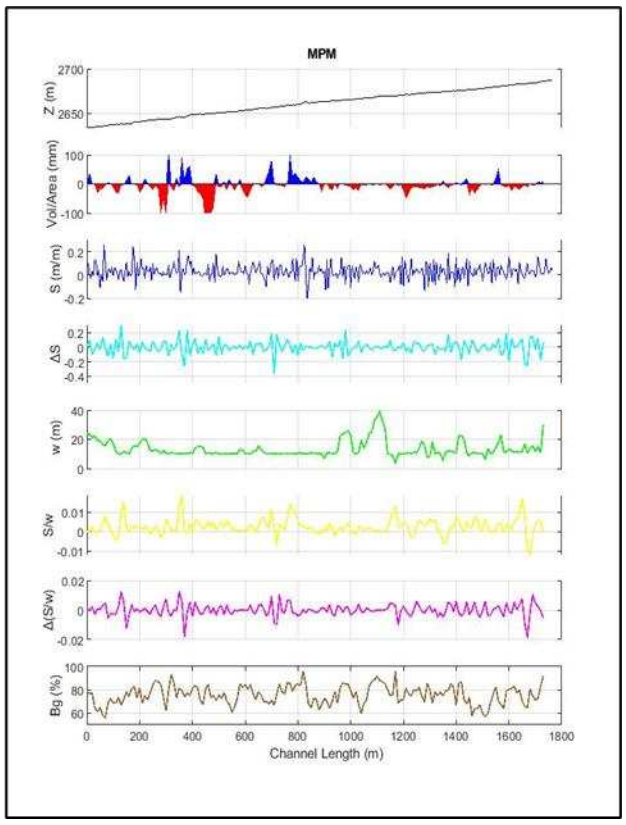
MPM
Z (m)
Vol/Area (mm)
S (m/m)
ΔS
w (m)
S/w
Δ(S/w)
Bg (%)
Channel Length (m)

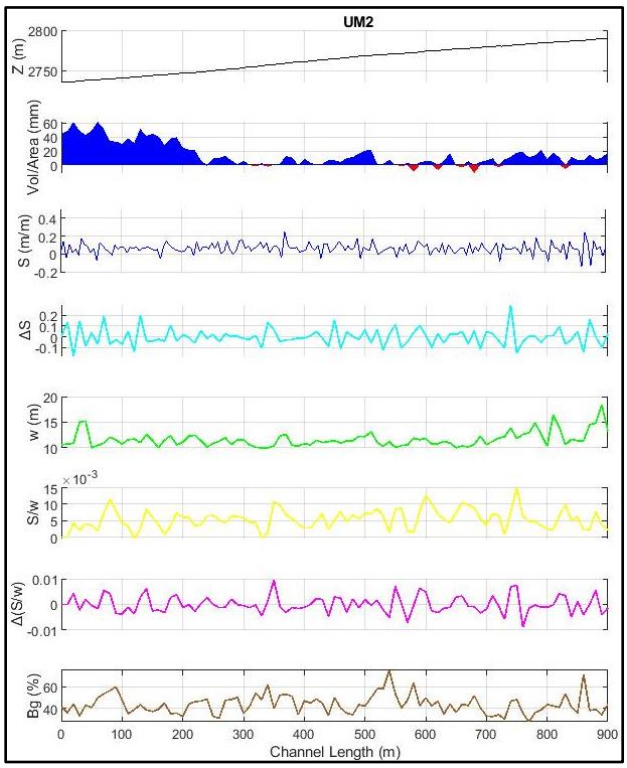
UM2
Z (m)
Vol/Area (mm)
S (m/m)
ΔS
w (m)
S/w
Δ(S/w)
Bg (%)
Channel Length (m)

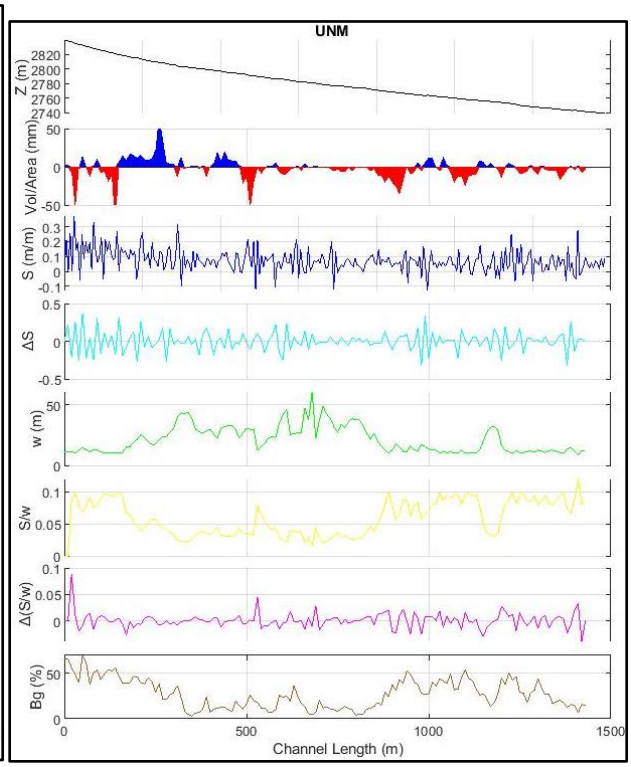
UNM
Z (m)
Vol/Area (mm)
S (m/m)
ΔS
w (m)
S/w
Δ(S/w)
Bg (%)
Channel Length (m)

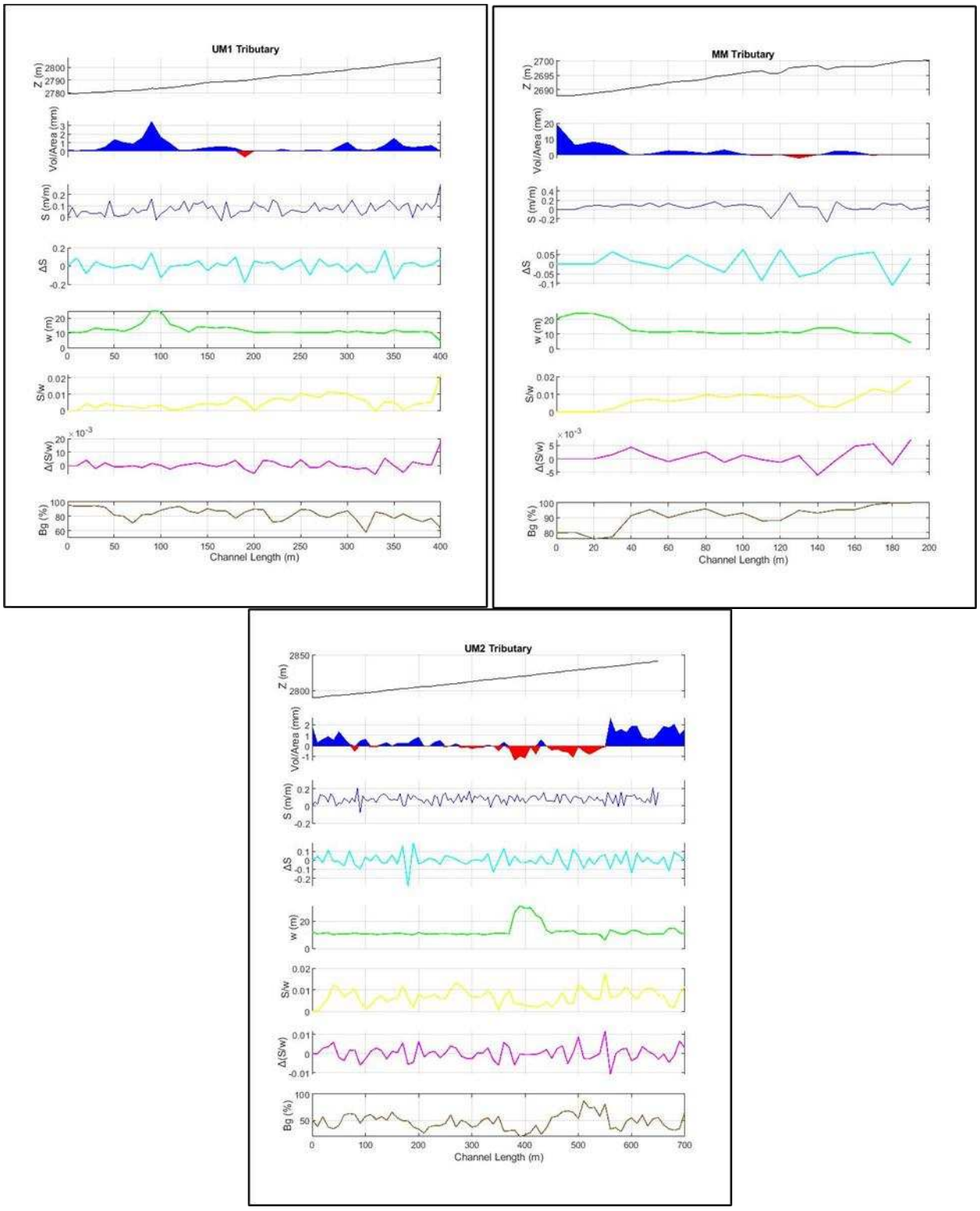

Appendix Figures 31-39: Longitudinal profiles of (top to bottom) elevation (*Z*), normalized volume, slope (*S*), change in slope (*ΔS*), width (*w*), slope divided by width (*S/w*), change in slope over width (*Δ(S/w)*), and bare ground percentage (BG)